Controls on spatial and temporal patterns of slope deformation in an Alpine valley

N. Oestreicher, S. Loew, C. Roques, J. Aaron, A. Gualandi, Laurent Longuevergne, P. Limpach, M. Hugentobler

Correspondence to:

N. Oestreicher,
Nicolas.Oestreicher@erdw.ethz.ch

Controls on Spatial and Temporal Patterns of Slope Deformation in an Alpine Valley

N. Oestreicher[1] , S. Loew[1] , C. Roques[1,2] , J. Aaron[1] , A. Gualandi[3] , L. Longuevergne[2] , P. Limpach[4] , and M. Hugentobler[1]

[1]Department of Earth Sciences, ETH Zürich, Zurich, Switzerland, [2]Centre for Hydrogeology and Geothermics (CHYN), University of Neuchâtel, Neuchâtel, Switzerland, [3]Istituto Nazionale di Geofisica e Vulcanologia (INGV), Osservatorio Nazionale Terremoti (ONT), Roma, Italy, [4]Department of Civil, Environmental and Geomatic Engineering, ETH Zürich, Zurich, Switzerland

Abstract A comprehensive surface displacement monitoring system installed in the recently deglaciated bedrock slopes of the Aletsch Valley shows systematic reversible motions at the annual scale. We explore potential drivers for this deformation signal and demonstrate that the main driver is pore pressure changes of groundwater in fractured granitic mountain slopes. The spatial pattern of these reversible annual deformations shows similar magnitudes and orientations for adjacent monitoring points, leading to the hypothesis that the annually reversible deformation is caused by slope-scale groundwater elevation changes and rock mass properties. Conversely, we show that the ground reaction to infiltration from snowmelt and summer rainstorms can be highly heterogeneous at local scale, and that brittle-ductile fault zones are key features for the groundwater pressure-related rock mass deformations. We also observe irreversible long-term trends (over the 6.5 years data set) of deformation in the Aletsch valley composed of a larger uplift than observed at our reference GNSS station in the Rhone valley, and horizontal displacements of the slopes towards the valley. These observations can be attributed respectively to the elastic bedrock rebound in response to current glacier mass downwasting of the Great Aletsch Glacier and gravitational slope deformations enabled by cyclic groundwater pressure-related rock mass fatigue in the fractured rock slopes.

Plain Language Summary Mountain ranges are subject to deformation due to tectonic forces, orogenesis, erosion, and gravity. Other factors can deform the slopes, such as atmospheric-driven thermal expansion and contraction, freeze-thaw in open fractures, and pore pressure variations. Close to retreating glaciers, the mechanical unloading of the ice body, and rapidly changing thermal and hydrologic conditions lead to deformation of the slopes. The difficulty resides in identifying the different factors contributing to the total deformation. We track surface displacements of fractured crystalline rock slopes adjacent to the Great Aletsch Glacier (Switzerland) tongue for more than six years at unprecedentedly high spatial and temporal resolutions. Our results demonstrate that groundwater is a critical driver of deformation. Centimetric reversible outward displacements are observed after the snowmelt season each year, followed by a seasonal recession to which are superimposed displacements caused by heavy rainfall-recharge events. Fault zones can be key features where most of the hydromechanical deformation occurs, and their geometry can control the direction of deformation. Glacier melting induces long-term trends of deformation. In addition, annual pore-pressure cycles lead to hydromechanical fatigue processes. This work opens a new vision on the spatial and temporal variability of processes responsible for bedrock deformation in paraglacial mountain slopes.

1. Introduction

Mountain slopes in paraglacial environments are perturbed when glaciers retreat. These perturbations induce surface displacements in adjacent slopes, which can be related to subsurface damage from fracture propagation (e.g., Grämiger et al., 2018; Grämiger et al., 2020) potentially leading to slope destabilization and collapse (e.g., Gischig et al., 2011; Loew et al., 2017). In addition to unloading due to glacier ice downwasting (e.g., Leith et al., 2014; Mey et al., 2016), seasonal deformation in response to temperature fluctuations (e.g., Hugentobler et al., 2020; Weber et al., 2019), snow load (e.g., Heki, 2001) and pore-pressure variations (e.g., Silverii et al., 2020) can contribute to long-term rock mass fatigue and progressive failure (Eberhardt et al., 2004; McColl, 2012).

Visualization: N. Oestreicher
Writing – original draft: N. Oestreicher
Writing – review & editing: N. Oestreicher, S. Loew, C. Roques, J. Aaron, A. Gualandi, L. Longuevergne, P. Limpach, M. Hugentobler

Many authors have analyzed cyclic displacements in alpine rock slopes with horizontal and vertical peak-to-peak amplitudes up to several centimeters (e.g., Grämiger et al., 2020; Loew et al., 2007; Oestreicher, 2018; Silverii et al., 2020). Yet, the contribution of the different factors described above in driving spatial and temporal variability in deformation remains poorly understood due to the limited access to long-term, high-resolution (both spatial and temporal) datasets. This paper describes and interprets one such data set in order to understand drivers of slope displacements in a paraglacial environment.

Cyclic rock slope deformations have been explained using a variety of short-term environmental drivers (Tsai, 2011). Seasonal temperature differences cause thermoelastic deformation of near-surface rocks (Prawirodirdjo et al., 2006; Tsai, 2011) which were observed at various places in mountain bedrock around the world (e.g., Collins & Stock, 2016; Collins et al., 2018; Gischig et al., 2011; Marmoni et al., 2020; Weber et al., 2017). Some of these studies report rock mass strains amounting to 500 μm/m for daily and seasonal temperature variations (Marmoni et al., 2020) and up to centimetric aperture variations of cracks in specific conditions (Collins & Stock, 2016; Collins et al., 2018). In gneisses and granites of the Swiss Alps, the maximum peak-to-peak amplitude of single crack deformation was measured with crack extensometers between 2 mm (Gischig et al., 2011) and 4 mm (Weber et al., 2017).

In alpine regions, frost-heave by ice segregation can induce large deformation of the ground if open fractures close to the surface are filled with water and exposed to freezing temperatures (Girard et al., 2013; Gruber & Haeberli, 2007; Matsuoka, 2008). In addition, the phase change of the water from liquid to solid implies a volume change of around 9% (Lundberg et al., 2016), which can increase the stress normal to the fracture walls and induce additional opening of fractures (Matsuoka, 2008; Musso Piantelli et al., 2020). Wegmann and Gudmundsson (1999) observed deformation in gneissic rock walls of the Aar massif explained by frost heave, and Matsuoka (2008) also described rainfall-related frost heave during spring and autumn, with freezing temperatures overnight.

Loading and unloading of the surface, often associated with hydrologic cycles, can induce cyclic displacements at continental scale (Van Dam et al., 2001) as well as the regional to local scale (Heki, 2001; Moreira et al., 2016). In mountainous regions, this process has been studied in both the Himalayan region (Bettinelli et al., 2008; Chanard et al., 2014; Flouzat et al., 2009; Gahalaut et al., 2017; Gautam et al., 2017), the Southern European Alps (Pintori et al., 2021; Serpelloni et al., 2018) and the Apennines (Silverii et al., 2019). In the Himalayan region, the peak-to-peak amplitude of the annual cyclic deformation of continuous Global Positioning System (cGPS) stations was measured up to 23.8 mm horizontally and 14.8 mm vertically at a cGPS station (Flouzat et al., 2009). The snow load in the mountains of northern Japan induces peak-to-peak deformation between mid-march and mid-august at cGPS stations up to around 17 mm vertically and around 5 mm horizontally (Heki, 2001). Additionally, Drouin et al. (2016) showed that surface loading by snow accumulation in winter is sufficient to produce measurable ground deformation in Iceland.

At depth, pore-pressure variations linked to changes in groundwater table elevations can induce a poroelastic response of the rock mass, for example, Wang (2000), after Biot (1941) and Rice and Cleary (1976). Hansmann et al. (2012) found that the annual groundwater table variations could explain the deformation observed in granitic rocks of the Gotthard massif. Valley perpendicular deformations, measured with robotic total positioning stations (TPS), were found to have amplitudes as high as 6 mm (as the TPS measured cumulative displacements from both sides of the valley, half of the annual amplitude of the signal is reported here). In the Southern European Alps and the Apennines, several studies hypothesize that pore pressure variations can explain the deformation of the region (e.g., Braitenberg et al., 2019; Grillo et al., 2018; Pintori et al., 2021; Serpelloni et al., 2018). Such deformation is mainly highlighted in karstic systems, where large variations of water level result in large localized deformation following heavy rainfall events (Braitenberg et al., 2019).

Over longer timescales, multiple environmental and tectonic factors drive mountain slope deformations in paraglacial environments (e.g., mass displacement in the asthenosphere, crustal tectonics, unloading by erosion, viscous, plastic, or elastic effects of deglaciation). These slow (decades to millions of years) changes are recorded as long-term trends in deformation time series. When interpreting these trends, the mixing of signals from various sources often makes it challenging to identify the most important causal factors (e.g., Sternai et al., 2019, and references therein). For the central Alps, Sternai et al. (2019) propose that around 70% of the measured uplift is caused by deglaciation (viscous isostatic rebound of the last glacial maximum (LGM) and elastic rebound from

current ice loss), and around 30% could be caused by deep mass movements in the asthenosphere. At the scale of a single valley, deglaciation can have multiple effects. During the ice retreat, elastic uplift of the ground has been observed using GNSS stations around large ice caps (e.g., Jiang et al., 2010; Ludwigsen et al., 2020). Further, in alpine valleys, the topography results in spatial variations of ice elevation, potentially inducing differential uplift (Ustaszewski et al., 2008). Grämiger et al. (2017) modeled the deformation response of a valley to the ice retreat from the LGM and showed that, in addition to differential uplift increasing towards the center of the valley, horizontal displacement of the valley flanks is expected. The motion is rotational, directed away from the valley center for the top parts of the slopes and towards it for the lower part (Grämiger et al., 2017; Figure 16). Accounting for thermomechanical effects during deglaciation, Grämiger et al. (2018) show that there is an increase in damage compared to a purely mechanical model and Grämiger et al. (2020) show a further increase in damage related to hydromechanical effects. An important observation from Grämiger et al. (2020) is that by changing the groundwater table in the slopes together with the change in ice elevation in their model, the top part of the slope also moves towards the center of the valley during deglaciation, contrarily to the purely mechanical model.

While all of the aforementioned processes can induce reversible surface deformations, it is often difficult to determine which process is dominant in alpine paraglacial environments. Separating the different sources requires high-resolution deformation monitoring, both temporal and spatial, and monitoring other environmental parameters such as climate and hydrology. So far, detailed studies of slope deformation following deglaciation have mainly focused on reactivation of slope instabilities (e.g., Glueer et al., 2020) or on deformation of sediment slopes (Cody et al., 2020). A study of bedrock deformation following deglaciation at the valley scale is missing.

The aim of this study is to assess the relative importance of various contributing factors to time-dependent surface deformation in alpine paraglacial environments, including near-surface air temperature, surface loads (e.g., ice, snow), and pore-pressure changes in the subsurface. We test the following hypotheses:

1. the strongest reversible slope deformations are caused by hydromechanically coupled deformations driven by seasonal groundwater storage-discharge cycles;
2. hydromechanically coupled deformations may have an irreversible component, which can be used to evaluate rockmass damage.

In addition we will explore the patterns of reversible and irreversible deformations and relate them to the geological and hydrological factors controlling their spatial and temporal variabilities at the hillslope to decameter scales. Conversely to previous studies performed in this study area which were mainly based on numerical models (e.g., Grämiger et al., 2020), this paper aims at identifying the driving mechanisms through an exhaustive analysis of a long-term data set now available.

2. Study Site Around the Tongue of the Great Aletsch Glacier and Installed Instrumentation

The study area is located in the central Swiss Alps, in the upper Valais, in a valley oriented SW-NE, roughly parallel to the adjacent Rhone valley (situated ∼5 km to the SW), but with a higher (800 masl) elevation of the valley bottom. The bedrock is formed of Paleozoic medium to high-grade metamorphic rocks (Schaltegger, 1994), and intrusions of central Aar granite, together with various types of dykes (Steck, 1983). These rocks underwent the Alpine ductile and brittle deformations and subsequent formation of a penetrative SW-NE striking Alpine foliation dipping steeply to the SE (Steck, 1983). The valley is occupied by the Great Aletsch Glacier (see Figure 1). Deposits of glacial till on bedrock in the study area can be related to three main stages: higher elevation (2,100–2,300 masl), well-vegetated Egesen moraines (Egesen glacial readvance stadial: ∼11 ky BP, (Grämiger et al., 2017; Ivy-Ochs et al., 2008)), lower elevation (1900–2,100 masl) and less vegetated Little Ice Age (LIA) moraines (recent glacier readvance, ∼*AD*1850, (Grämiger et al., 2017; Mann et al., 2009)), and recent, usually relatively thin till deposits from the current glacier retreat. The latter are sparsely vegetated. The area monitored for surface deformation covers 12.8 km², of which 9% is ice-covered, 26% is covered by moraines and debris and 65% is partly exposed bedrock.

Numerous slope instabilities have been mapped and analyzed in the valley (Glueer et al., 2019; Kos et al., 2016; Strozzi et al., 2010). The active Driest and Moosfluh landslides (see Figure 2) are situated around the current position of the glacier tongue and show displacements of a few millimeters per year up to meters per day for part of
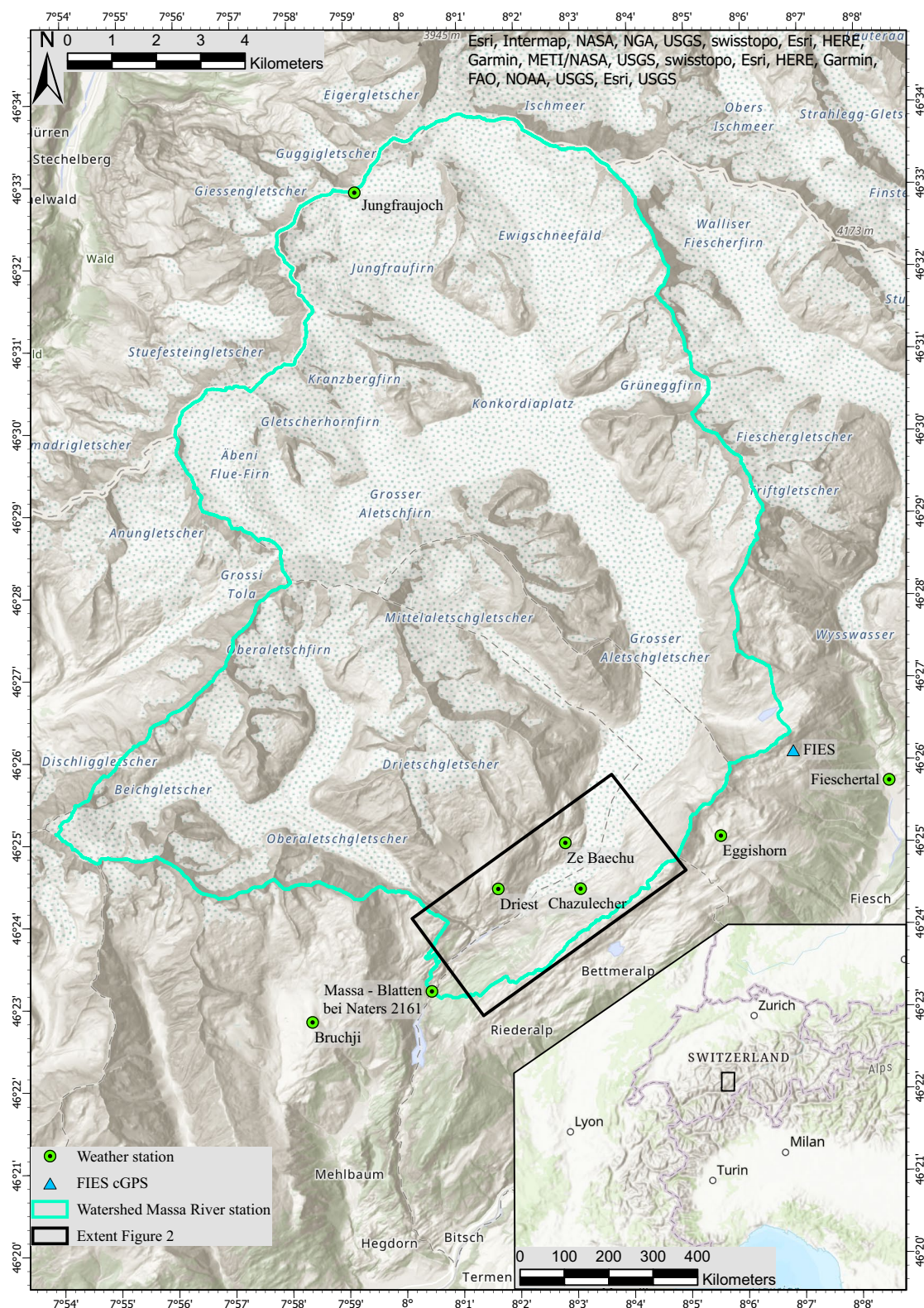
Figure 1. Topographic map of the central European Alps. The weather stations used (green points) and the continuous Global Positioning System station FIES (blue triangle) are shown. The black rectangle is the extent of Figure 2 and the inset shows the location of this map in the European Alps.
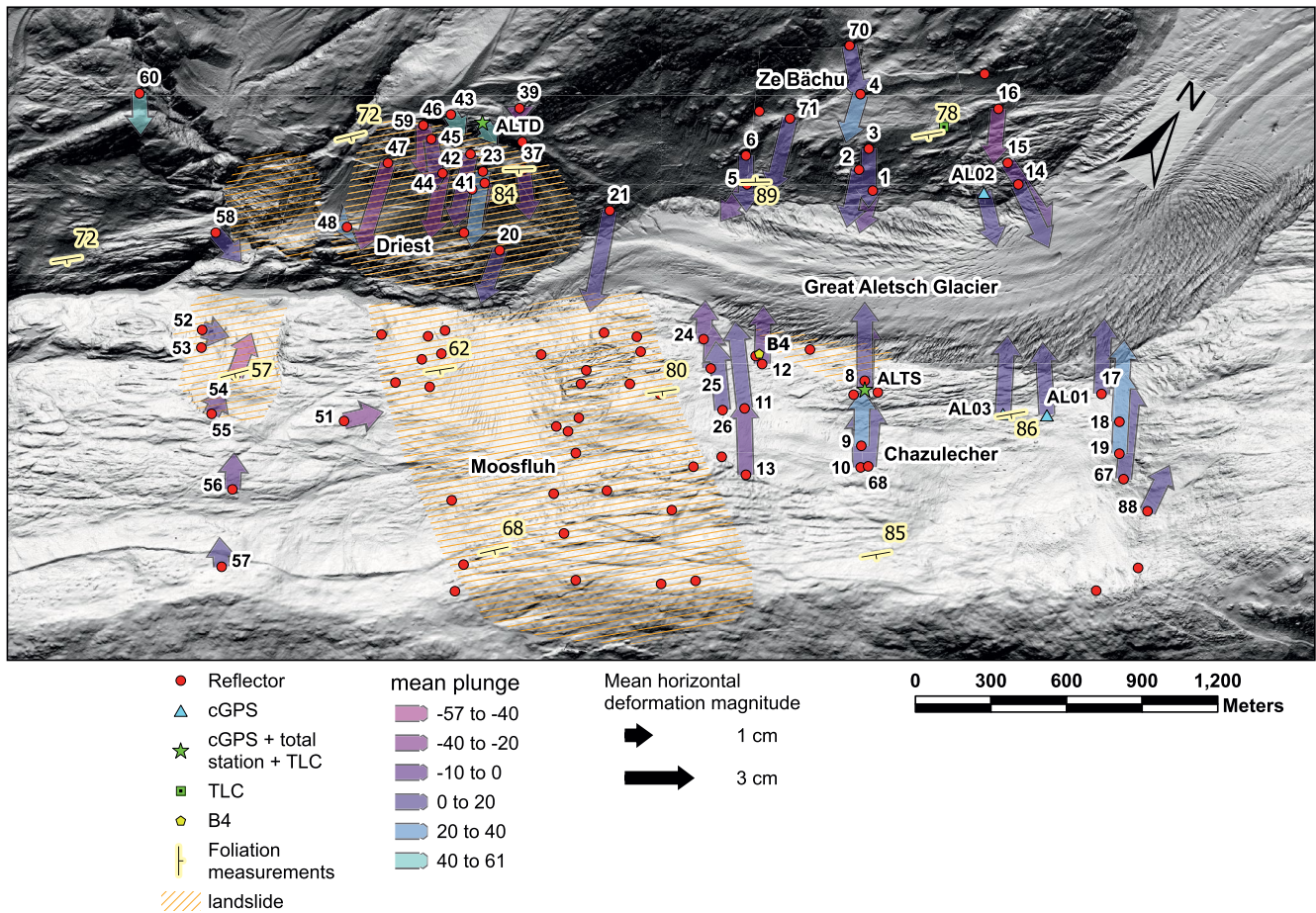
Figure 2. Map of study area with monitoring stations and known slope instabilities. Arrows are the average displacement in Spring exaggerated 10'000 times. Colors of arrows represent the plunge angle. Structural measurements of the main foliation are in yellow, based on a compilation of Grämiger et al. (2017); Glueer et al. (2019) and authors' own field mapping data. See Figure 1 for the location of this map.

the Moosfluh landslide in September 2016 (Glueer et al., 2019). The great Aletsch glacier is currently retreating at an average rate of ∼50 m/y for the years 2000–2018 (GLAMOS, 2020), and its tongue retreated around 3 km since the LIA. Ice downwasting in the study area is in the order of 10 m per year (Hugentobler et al., 2020). The mean annual temperature in the study area is $3.2 \pm 0.5°C$ at the Chazulecher station (1971 masl, Northwest-facing slope) and $4.6 \pm 2.0°C$ at the Driest station (2,173 masl, Southeast-facing slope) for the period 2013–2020. The mean annual precipitation as measured at the nearby Bruchji station (2,300 masl, South-facing slope) since 2013 is 999 ± 139 mm of which a significant proportion falls as snow and accumulates during the cold months. The nearby SLF Eggishorn station (2,495 masl, South-facing slope) measured a mean annual maximum snow depth of 2.15 ± 0.48 m since 1994, and at the SLF Belalp station (2,554 masl, South-facing slope), the mean annual maximum snow depth was 2.52 ± 0.50 m since 2009. For the location of the weather stations used here, see Figure 1 and Table 1.

The groundwater in the fractured rock mass is fed by water infiltrating from the surface. The availability of water for infiltration is strongly dependent on the temperature in alpine environments, as water is stored as snow during most of the winter, with little infiltration, and delivered quickly during snowmelt in spring. Significant groundwater level changes are typically observed at this time of year, resulting in an annual cyclicity in groundwater storage (de Palézieux & Loew, 2019). During summer, infiltration happens mainly during rainstorms, which are not very frequent, as the climate is dry in the central valleys of the Alps. At the Massa river monitoring station (see Figure 1), the flow in the river fluctuates from low flow in February, with an average of 0.32 ± 0.12 m³/s and extrema around 0.13 m³/s and high flow in July with an average of 44.55 ± 14.88 m³/s and extrema around 97 m³/s (see

Table 1
Weather Data Used in This Study

Variable	Station	Latitude	Longitude	Altitude (masl)
Rainfall	Bruchji	N46° 22' 46"	E007° 58' 18"	2,300
Rainfall	Fieschertal	N46° 25' 40"	E008° 08' 28"	1175
Snow height	Belalp	N46° 23' 41"	E007° 58' 27"	2,554
Snow height	Eggishorn	N46° 25' 00"	E008° 05' 30"	2,495
Temperature	Eggishorn	N46° 25' 00"	E008° 05' 30"	2,495
Temperature	Jungfraujoch	N46° 32' 51"	E007° 59' 08"	3,571
Massa River flow	Massa-Blatten bei Naters 2161	N46° 23' 08"	E008° 00' 24"	1446

also Figure A1). A trend towards earlier snowmelt and larger high flows in summer, caused by increased melting of the glacier under the current climate warming, is predicted in high-alpine catchments (Muelchi et al., 2021).

An extensive surface displacement monitoring system was installed in 2013 and continuously expanded and maintained since (Glueer et al., 2020, 2021), m high metallic pole of 21 cm diameter, bolted in bedrock (Frukacz et al., 2017). To prevent temperature and wind-related movements of the poles, these are protected by a second larger metallic tube (Frukacz et al., 2017). The monument of the station AL03 consists of a 1 m high and 21 cm in diameter metallic pole bolted in the bedrock. Finally, the stations AL01 and AL02 monuments are 1.2 m high and 20 cm in diameter steel pillars with solar panels attached to their sides (Limpach et al., 2016).

Two total stations were installed on opposite valley flanks directly below the GPS stations of ALTS and ALTD, monitoring their position (see Figure 2). A Leica TPS1200 was installed at Chazulecher station, point ALTS, and a Leica TM50 station was installed at Driest, point ALTD (Frukacz et al., 2017; Glueer et al., 2020). These stations track 93 reflectors that have been installed on both unstable ground (active landslides) and adjacent stable bedrock (see Figure 2). Reflectors are equipped with a stainless steel roof to protect against snow load, snow creep, and small rockfalls. The air temperature and atmospheric pressure are monitored at the two total stations for data correction, and a nearby weather station is situated in Ze Bächu. In addition, three bedrock monitoring boreholes were drilled in 2017 close to the left glacier margin and described by Hugentobler et al. (2020). Here, only the piezometric data from borehole B4 are shown. The location of B4 is shown in Figure 2. The borehole B4 is 44.4 m deep, fully grouted after instrumentation with a 0.5 m long sand filter at the location of the piezometer (43.75 m under the surface). Boreholes B2 and B6 are not included in the analysis here, respectively because of a faulty sensor, and a position on a dormant instability with probable influence from surface water infiltrating through highly transmissive fractures above the borehole B6. B4 is considered more representative of the rock slope conditions in the study area. More details on the boreholes setup and data are available in Hugentobler et al. (2020).

3. Data and Methods

3.1. Surface Displacement

The five cGPS stations installed on both flanks of the valley are equipped with low-cost single-frequency GPS devices. The GPS data processing is based on the Bernese GNSS software, using differential carrier phase techniques. Daily static coordinates are computed with respect to the geodetic dual-frequency GNSS station FIES situated close to Fiescheralp (Limpach et al., 2016). The relatively short baselines (5.0–7.4 km) between the GPS stations and the reference station FIES allow the mitigation of ionospheric effects by differential processing, and hence the use of single-frequency GPS receivers. The station FIES is part of a regional network of 10 geodetic reference stations operated by the Institute of Geodesy and Photogrammetry of ETH Zurich. This regional dual-frequency GNSS network is continuously processed together with stations of the Swiss national network of GNSS reference stations AGNES (Automated GNSS Network for Switzerland) from Swisstopo. The reference station FIES is subject to similar cyclic motions as studied here. Its position is continuously computed with respect to the Swisstopo station Hohtenn (HOHT) from the AGNES network, situated in the Rhone valley. This allows to eliminate station FIES's motion and to reference the GPS stations near the glacier to the station HOHT in the Rhone

valley. A direct vector between the station HOHT and the stations near the glacier would yield much longer baselines prone to ionospheric delay errors with the single-frequency receivers. The effect of the temperature on the monuments has been investigated by Frukacz et al. (2017) and shown to be below the noise level of the stations.

At the total stations, interruptions of data acquisition sometimes occur during periods where the station is snow or ice-covered and occasionally because of rockfalls or snow avalanches covering or destroying reflectors. Fog in the valley, particularly in autumn, also reduces the visibility of reflectors situated far from the total stations (up to 2 km). Each point is measured multiple times at night, when air temperature gradients along the ray path and wind have a minimal influence on the measurement. The total station records the distance to the reflector, the horizontal angle from North and the vertical angle on each face of the instrument, in order to average the angles obtained and reduce instrumental errors. Then, the measured distance to the prism is corrected for atmospheric temperature effects using correction factors provided by Leica Geosystems AG (2013).

Both angles (horizontal and vertical) are low-pass filtered to reduce noise and combined with the distance measurement to infer the position of the prism relative to the total station. The station regularly checks its alignment to one of the reflectors, considered as reference, to prevent drift caused by mechanical errors. However, the reference point is not considered as stable and is also included in the analysis here. For ALTD, it is point 39 and for ALTS, point 10 until 2019 and 68 afterward (see Figure 2). Point 68 is located close to 10 but is less often snow-covered, which is important to avoid drift of the angular measurements during winter. Therefore, we decided to include reflector 68 as a reference point in 2019. We noticed an increase in instrumental noise when using two reference points and switched to only one (point 68) after a few months. We discard data from this period in our statistical analysis to overcome potential issues related to this instrumental noise. We average all night-time measurements between 10 p.m. and 6 a.m. to calculate daily solutions of each prism position. Because the total station cannot be considered stable and is subject to a similar motion as the reflectors, we correct the relative position obtained with the low-pass filtered GPS position of the total station to get the absolute position of each prism. For filtering of the position time series, we apply a Butterworth low-pass filter of third order with a cutting frequency of 3.858×10^{-7} Hz (corresponding to a period of 1 month, see Figure 3). These parameters are used for low-pass filtering of daily sampled data throughout this paper if not specified otherwise.

The fast displacement in spring (see Figure 3) is calculated for each point with a peak-to-peak amplitude of the seasonality larger than 5 mm. The points corresponding to the start and end of the spring displacement are identified on the time series for each year in the record. We take the average displacement obtained between these two times for all available years in record, at each point. The results of this analysis is shown in Figure 2.

To extract information from the displacement time series and separate the signal coming from different temporally independent sources, we use a statistical method, the Variational Bayesian Independent Component Analysis (vbICA). The vbICA is described by (Choudrey & Roberts, 2003) and adapted to the study of geodetic position time series with gaps by Gualandi et al. (2016). We use the two-dimensional horizontal displacement time series (east, north) for reflectors and cGPS stations that do not have large data gaps (exceeding 20% of the time series). We do not use the vertical component of displacement, as the noise level is higher in the vertical (see Figure 3), and most of the displacement is horizontal (see plunge angles in Figure 2). The resulting time series for each Independent Component (IC) are then compared with environmental variables and geologic knowledge to explain better the original deformation observed. We select the number of components to retain via an F-test, and we test different initialization hyper-parameters. We impose small a priori variance on the mixing matrix hyper-parameters to stabilize the solution, as described in Gualandi and Liu (2021), for example, in Table S1. Here we use values of 1×10^{-3} and 1×10^{3} for the hyperparameters b_{α_0} and c_{α_0} respectively.

3.2. Strain Analysis

Using the distance measurement of the total station, we can directly infer strain between two points on the slopes. This technique has the advantage of increasing the signal-to-noise ratio, as it does not use the angular calculations of the TPS or the absolute positioning from GPS. For points situated far from the total station, a daily solution of distance measurement is used. High-resolution strain measurements are performed between close reflectors and the total stations. Hourly temperature-corrected distance measurements to the total station, including measurements during the day, offer a data set similar to the one we would obtain from low-accuracy extensometers.
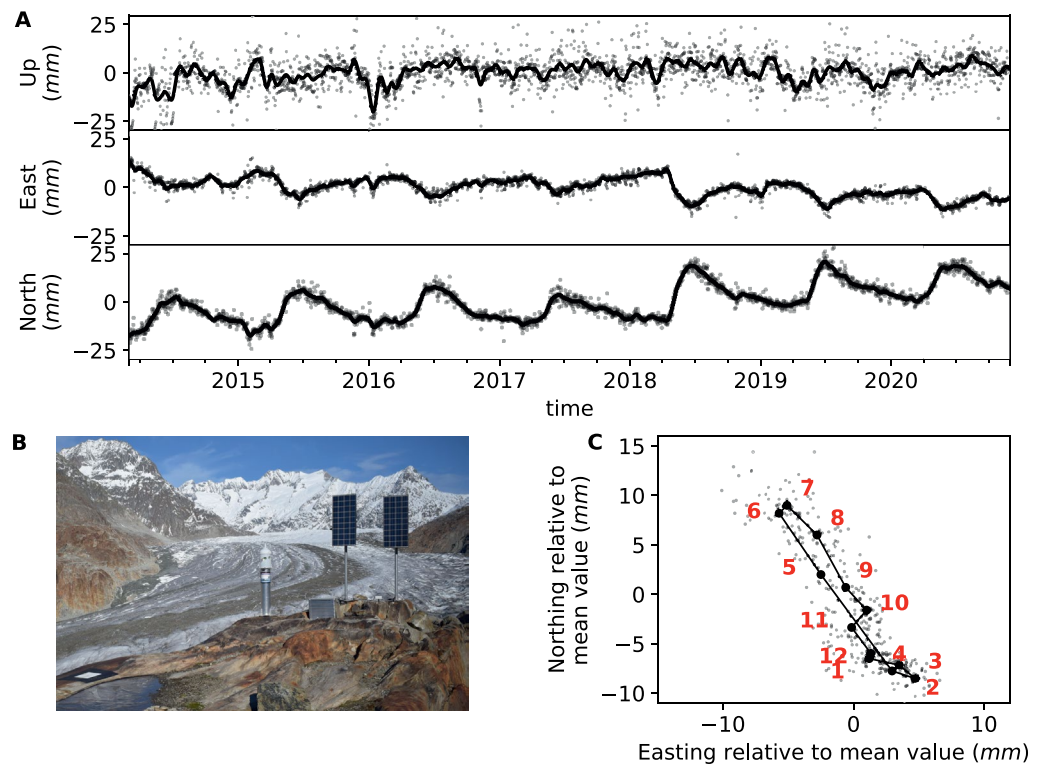
Figure 3. Example of time series for a continuous Global Positioning System situated at the Chazulecher station (ALTS). (a) Three spatial components of displacement relative to Hohtenn (HOHT, gray dots) with filtered data (black line). (b) Picture of the station and its surroundings, view to NE. The GPS is on top of the total station (left mast). (c) Horizontal displacement seen from top. Gray points are average values from ordinal days after linear detrending of the time series. Black points are average monthly values, labeled in red. The quicker deformation in spring to early summer to the NNW is followed by a slower, more gradual deformation in the opposite direction during the rest of the year. The cyclic deformation is mainly in the horizontal direction, although the higher noise in the vertical component might prevent the detection of annual cyclicity.

These datasets are used to analyze smaller and shorter relative displacements of the prisms and compared with environmental variables (e.g., air temperature, rainfall, snowfall).

3.3. Weather and Climate

Time series of weather variables (air temperature, rainfall, snowfall, atmospheric pressure) are taken from nearby MeteoSwiss stations located outside of the study area (see Table 1). The main stations used are Belalp and Egg-ishorn. The water level and temperature in the Massa river, at the outlet of the Great Aletsch, Oberaletsch, and Driest glaciers are taken from a station managed by the Federal Office of the Environment (FOEN). Inside the study area, a weather station is installed on the South-facing slope at Ze Bächu and informs on air temperature, atmospheric pressure, bolts of lightning, wind direction and speed, and solar radiation with a 15 min sampling interval. Air temperature and atmospheric pressure are also measured at both total stations in Chazulecher and Driest, with an hourly sampling interval.

The spatial variations of snow cover during the melting season are monitored with two time-lapse cameras, each facing one valley flank, using the method described in Aaron et al. (2021). The slopes are partitioned in sectors based on their orientation and elevation characteristics, and the degree-day method (Rango & Martinec, 1995) is applied on each sector, backward in time from the last day with snow in the area, to get an approximate snowmelt timing and amount during the spring snow melting season. A degree-day factor of 0.08 cm/(°C d) is applied during winter and until March and a degree-day factor of 0.4 cm/(°C d) is applied after the start of April, following (Rango & Martinec, 1995). An elevation-dependent temperature correction of 7.2×10^{-3} °C/m is applied, based on the temperature gradient observed between nearby measuring stations.
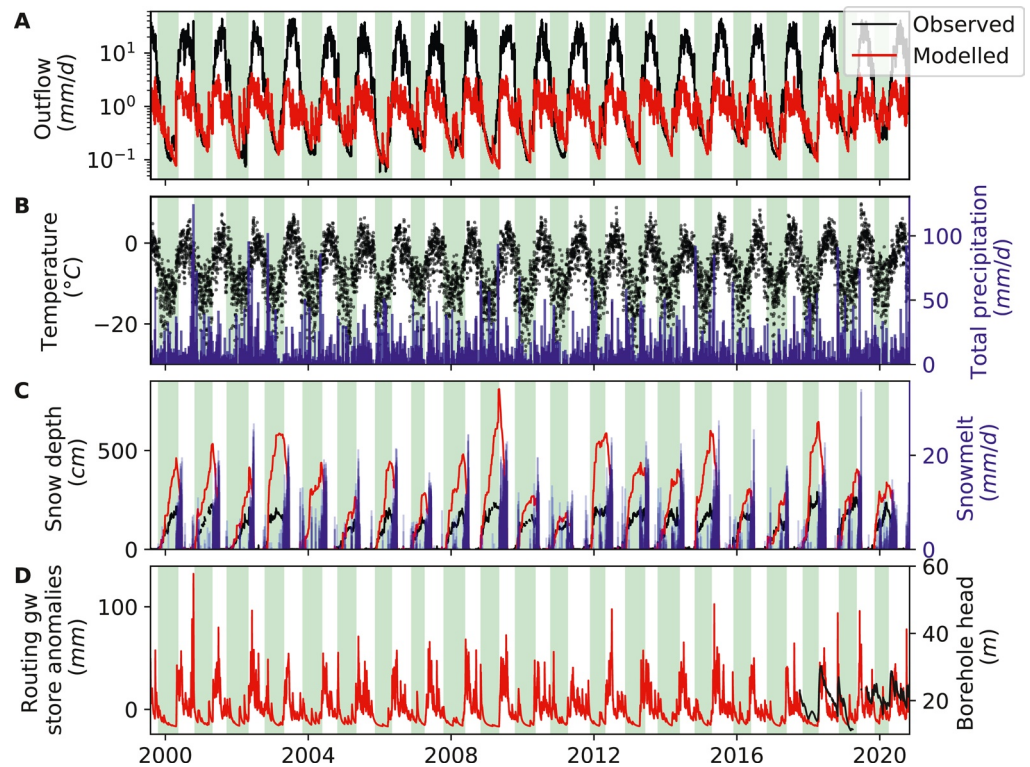
Figure 4. Results of the GR5J model for groundwater storage estimation at catchment scale. (a) Flow in the Massa river, normalized by the size of the catchment, with observations (black) and model (red). Calibration periods are shown in green. (b) Temperature at the Jungfraujoch station (black) and precipitation at the Fiesch station (blue). (c) Snow depth at the Eggishorn station (black), modeled from GR5J for the entire catchment (red) and modeled snowmelt (blue). (d) Anomalies to the mean of the groundwater storage modeled (red) and observed head in the borehole B4 (black).

3.4. Groundwater Monitoring and Modeling

The variations of groundwater heads are monitored in the borehole B4 (Figure 2, the reader is refered to Hugentobler et al. (2020) for more details on the borehole monitoring system). Groundwater storage-discharge dynamics is modeled at the catchment scale with the lumped rainfall-runoff model GR5J (Pushpalatha et al., 2011), modified to include a snowmelt routine based on the degree-day method (Valéry et al., 2014). The model is calibrated using the variations of stream discharge in the Massa river, with air temperature at the Jungfraujoch, precipitation from the Fieschertal, and solar radiation from the Jungfraujoch station as inputs. GR5J resolves the rainfall partitioning between evapotranspiration, quick (surface) and slow (subsurface) flow paths. From the air temperature and sunshine duration, we calculate the potential evapotranspiration with the Turc method (Turc, 1961). Modeled snow accumulation and melting rates were validated on measured snow depth at the nearby Eggishorn station. The model is calibrated on the river discharge by minimizing the Nash-Sutcliffe Efficiency index (Nash & Sutcliffe, 1970). It is computed over the logarithm of the discharge data to focus the importance of the low flows when groundwater is the main contributor to stream discharge.

In the case of the Aletsch valley, the Massa river gauge has a large catchment of ~191 km², with a significant part covered by glaciers (see Figure 1). The river discharge dynamics is highly influenced by the meltwater from the glaciers inducing high flow regimes during summer and low flows in winter (see Figure A1). To limit the influence of the glacier melting, we calibrated the GR5J model only during winter periods, when glacier contribution to river discharge appears minimal (see Figure 4). Details of the calibration process are compiled in Appendix A.

3.5. Geological Mapping

Structural field mapping was done using two applications; Fieldmove and Fulcrum. A drone (DJI Phantom v4) was used to acquire a high-resolution surface model around the total station of Chazulecher. The flights were

prepared with the software DJI Flight Planner, and Litchi was used to control the drone on-site. Then, the 3D model was computed with Agisoft Metashape, and an orthophoto, digital terrain model (DTM), and mesh were produced. Fractures were then manually digitized in ArcGIS Pro from the orthophoto, and shear zones orientations were computed in Virtual Reality Geological Studio (VRGS), and with a hand-held compass in the field.

4. Results

4.1. Surface Displacement: Temporal and Spatial Patterns

The installed cGPS stations and TPS reflectors record significant reversible and long-term ground surface displacements. On both sides of the glacier, points attached to bedrock exhibit at least three types of motion exceeding the noise level. These are (a) reversible short-term displacement, over a few days to a few weeks, (b) annually reversible displacement, and (c) apparently irreversible displacement over the period of recording. We exclude points from the center of the fast moving Moosfluh landslide because the displacement of these points is strongly dominated by the landslide motion and has already been thoroughly studied in a previous paper (Glueer et al., 2020).

The three types of motion we observe are well demonstrated by the cGPS station ALTS, shown in Figure 3, in the top three panels. This cGPS station exhibits a long-term trend upwards at an average rate of 1.0 mm/yr, to the North with 3.0 mm/yr and to the West with 1.5 mm/yr over the period 2014–2020. Seasonal cycles with a peak-to-peak amplitude of 24.8 ± 5.7 mm are visible. The seasonal displacement takes place on a plane close to horizontal, but it has to be noted that a higher noise level in the vertical component of the cGPS might hide a vertical seasonal displacement component. The bottom right of Figure 3 shows the annual displacement of the GPS antenna in plan view. The East and North components were detrended and averaged per ordinal day (light gray) and month (black dots). The station moves rapidly to the North-West in spring (April to June) and moves back during summer, autumn, and winter (August to December), decreasing velocity over the year. A picture of the station is shown at the bottom left of Figure 3, and the map (Figure 2) indicates that the station is moving towards the valley center (i.e., towards the glacier) in spring, and away from it during summer-autumn.

The peak-to-peak amplitudes of all points situated outside of the large Moosfluh instability where a seasonal signal was detected are shown as arrows in Figure 2. Most of the points move towards the center of the valley in spring and away from it in summer-autumn. The points that are near each other show similarities, both in terms of direction of motion and magnitude. In general, points on the North-facing slope move to the NNW, and points on the South-facing slope move the SSE with slightly more variation in the direction. Points 14–19 are located where the valley axis is rotating. While the direction of displacement (121 ± 9°) is rotating with the slope dip direction (176 ± 66°) in the zone of points 14, 15 and AL02, the zone around points 17–19, 69 and 88 moves in a direction of 333 ± 9° while the slope dip direction is oriented 276 ± 36° at this location. Hence, the motion of these points is not slope-perpendicular. The points on the North-facing slope seem consistently moving perpendicularly to the orientation of the main alpine foliation (mean dip/dip direction of 85°/136°, see Figure 1). The majority of the points have a plunge angle around 0°; hence they move almost horizontally. We note that the increased noise in the vertical component of displacement could hide small variations of plunge between points.

We extract ICs statistically from the position time series of cGPS and TPS, using the vbICA method. These components can be linearly recombined to explain the observations. We show the results of the vbICA with four ICs on Figure 5. To obtain the contribution of each IC to the original data, we multiply the spatial distribution (maps in Figure 5) by the corresponding temporal functions. In other words, to obtain the displacement at a given station associated with a specific IC, we have to multiply the spatial response shown in the map by the corresponding temporal function. The approach eases a physical interpretation of the observed signal, separating it into various statistically independent contributions. The first IC exhibits a long-term trend, with a strong acceleration in late 2016 and logarithmic deceleration afterward. The timing corresponds to the acceleration phase of the Moosfluh landslide (Glueer et al., 2019), and the map shows that this component is very active for points close to the Moosfluh instability. Some outliers, as well as some deviations to this trend in 2018, are observed. They are considered as caused by noise in the time series. During this time, a data gap affecting both total stations left only the cGPS stations working. The algorithm is affected, and this time period is not representative of the slope motion.
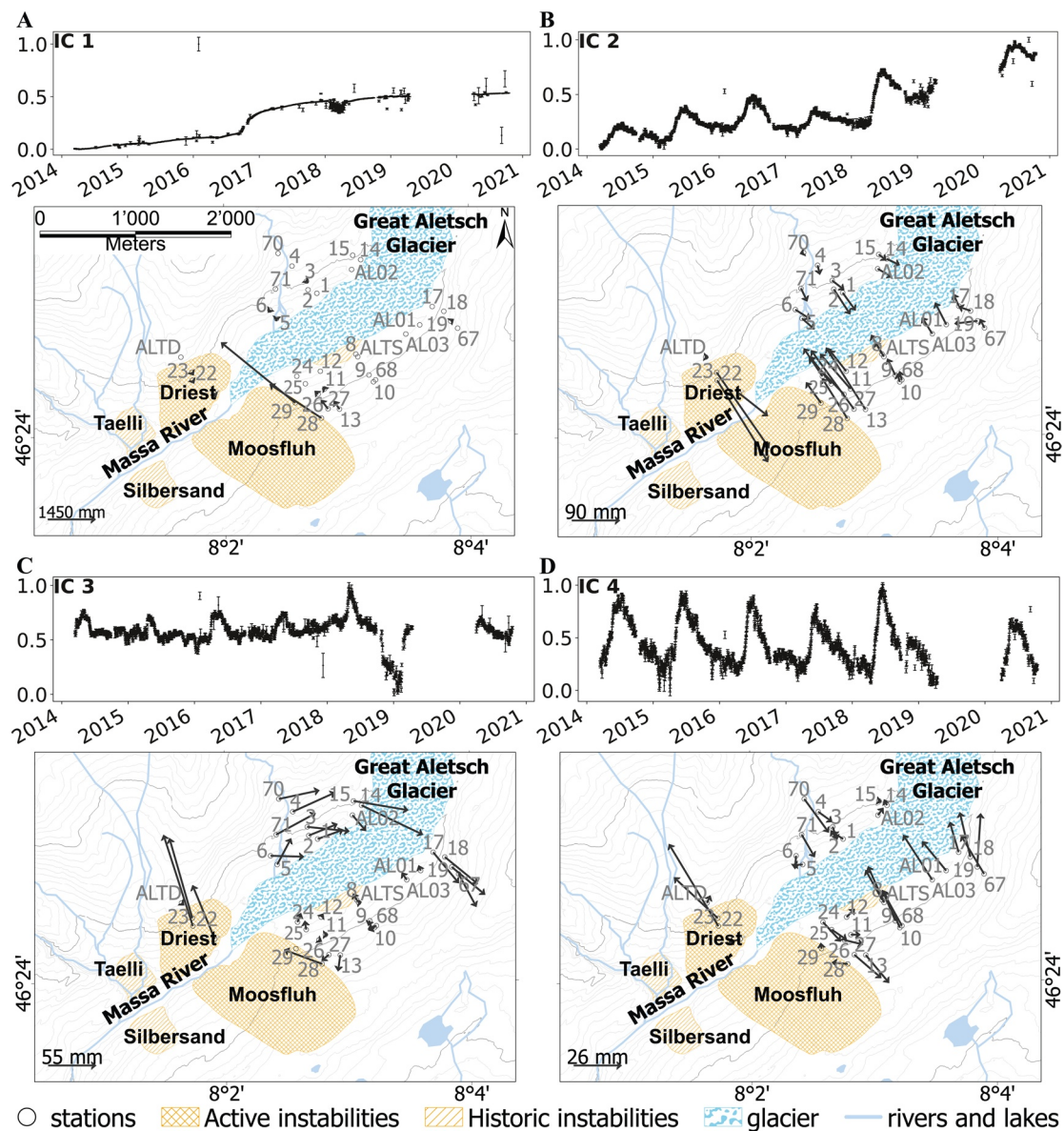
Figure 5. Results of the vbICA analysis with four independent components (a): IC1, (b) IC2, (c) IC3 and (d) IC4. The temporal function of each component is shown above its respective spatial distribution at points included in the analysis (gray labels).

The second IC shows a positive long-term trend, as well as cycles with an annual periodicity and variable amplitude between years (see Figure 5). This component is identified at all stations on the map, with a direction towards the center of the valley. The magnitude of the component is increasing towards the Southwest, where the large instabilities of Driest and Moosfluh are situated.

The third IC shows annual cycles with short positive incursions in spring followed by motion in the opposite direction and a bigger event with opposite direction in 2019 (see Figure 5). The magnitude of the component is increasing with the distance to the total station (point ALTS on the map), and the direction exhibits a rotation of the points around the total station. This peculiar behavior could be caused by a rotation of the station on its axis, with repercussion of this movement to all the reflectors. The period with strong negative incursion in 2019 is simultaneous with the noisier period caused by the change of reference points at the total station already discussed in Section 3.1. In addition to the detection of the angular noise of 2019, it is also possible that the vbICA method incorporates in the third IC some of the strong annual signal in spring, or another related deformation signal.
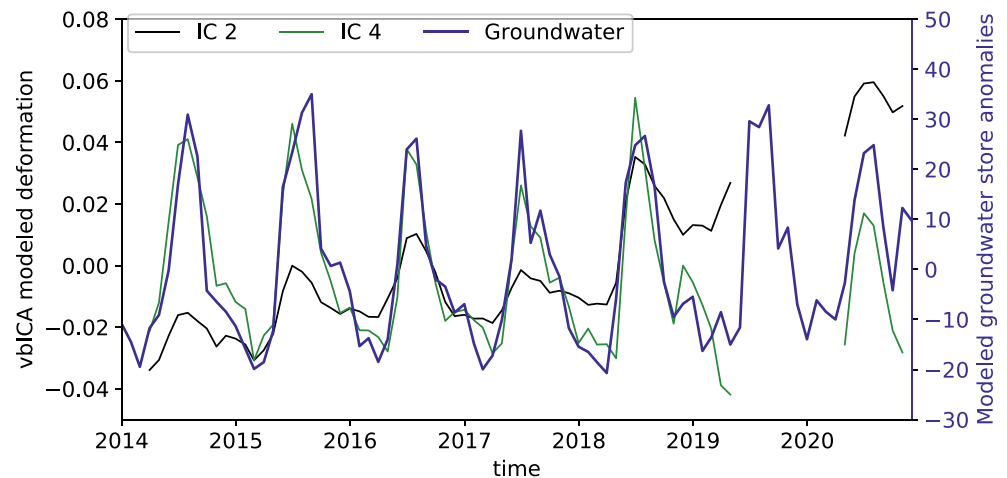
Figure 6. Comparison between the ground deformation extracted from the vbICA method (IC2, black and IC4, green) and groundwater estimated with the GR5J model (blue), normalised with the mean and standard deviation of the timeseries.

The fourth IC exhibits similar annual cycles as the second component (see Figures 5 and 6) but does not include a long-term trend. The direction of the motion is opposite to the one of the second IC for points close to the landslides and in the same direction as the second IC for other points. The magnitude is larger for points on the Northwest facing slope, and point 22 on the Driest landslide. It is possible that both IC2 and IC4 partially describe motion from the same source. IC4 could correct the amplitude of the annual reversible displacement of the points where IC2 could not explain the entire reversible and irreversible signal. For example, points close to the Moosfluh landslide and on the Driest landslide often exhibit opposite directions of motion for IC4 and IC2. Therefore, IC4 reduces the amplitude of the annual reversible displacement at these points, where IC2 has large amplitudes due to a strong irreversible component of displacement. For the North-East part of the study area, instead, IC4 and IC2 are oriented in a similar direction. Therefore IC4 serves as a reinforcement of the annual reversible displacement where IC2 exhibits lower amplitudes, because the irreversible component of displacement is smaller at these points. Both components could represent a single source responsible for both annually reversible and irreversible displacements, or of two separate sources that are difficult to differentiate.

In Figure 6, we show groundwater storage variations obtained from the GR5J model. Seasonal cycles are caused by increased infiltration and recharge during snowmelt in spring. During summer, autumn, and winter, the groundwater storage is depleting. Interannual variations in the magnitude of groundwater storage variations are linked to differences in the snowpack between years. The calibration periods of the model are displayed in green in Figure 4. Differences between the groundwater store modeled and the groundwater head observed in the borehole B4 in Figure 4 can be caused by the different scales of observation. Observed groundwater level variations can be very local, while modeled groundwater storage changes are representative of the whole basin. However, relating the groundwater store change in spring (~70 mm) with the local water head change in the borehole (~15 m) gives an estimated porosity of 0.5%, which is reasonable for the shallow fractured gneisses and granites of the Aar massif (Masset & Loew, 2010). The ICs 2 and 4, exhibiting the annual cycles, are shown in Figure 6 for comparison. There is a significant correlation between the general trend of monthly catchment-scale groundwater storage and deformation in the study area, both in terms of timing and inter-annual magnitude variations. Pearson's correlation coefficient between groundwater storage and the ICs 2 and 4 of ground deformation are respectively 0.37 and 0.77 at a monthly resolution. The long-term trend in IC2 reduces the correlation coefficient with the groundwater storage.

4.2. Strain Measurements

In Figure 7, we show strain measured across the valley, from the Chazulecher total station to the reflector point number 2. We choose this reflector because its direction from the total station is parallel to the main direction of annually cyclic deformation in this part of the valley (see Figure 2) and because it has relatively few periods of missing data. Also, the strain across the valley integrates the deformation from both slopes, increasing the
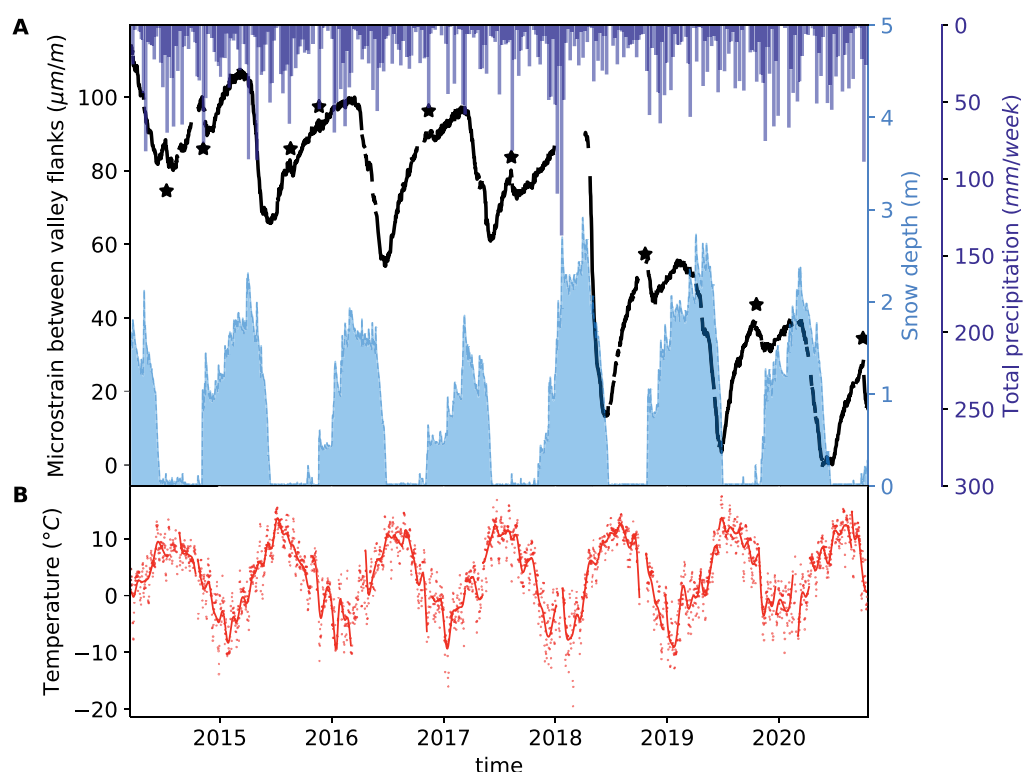
Figure 7. (a) Distance measurement timeseries, between two points on each side of the valley (here, reflector number 2 and the total station in Chazulecher, black). The distance measurement is corrected for effect of air temperature, atmospheric pressure and air humidity. Snow depth (light blue, Eggishorn MeteoSwiss station) and rainfall per day (deep blue, Bruchji Meteoswiss station) are also shown, as well as short periods of deformation during summer/autumn (stars). (b) Daily mean temperature (points) and low-pass filtered data (line) at the Chazulecher station.

amplitude of the annual cycles and the signal-to-noise ratio. A clear long-term trend is visible, with a shortening of the distance between these two points of 11.3 mm/yr on average between 2014 and 2020. The annual reversible cycles described in the previous section are again evident in this data set, with a shortening every year in spring followed by extension during the rest of the year. The magnitude of deformation in spring can be related to the magnitude of non-recovered deformation, calculated from winter times each year (see Table 2). In Table 2, the spring deformation corresponds to the peak-to-trough deformation from Figure 7 between the end of winter and the start of summer, while the non-recovered deformation corresponds to the peak-to-peak deformation from one end of winter to the next.

The deformation of the valley in spring is synchronous with the onset of snowmelt in the valley, as shown in Figure 7. However, the subsequent opening of the valley starts well before the snow begins to accumulate again on the slopes, discarding loading of the surface by snow accumulation has the main driver of the deformation. The temperature is also shown in Figure 7. The Pearson's correlation coefficient between strain and temperature is −0.39, and seasonality is visible for both variables. However, the asymmetry in the deformation signal is not reproduced in the temperature, which exhibits a more sinusoidal shape in general. In addition, some small reversible incursions in strain (marked with stars in Figure 7) cannot be related to changes in air temperature or snowpack. These seem to be linked to periods of heavy rainfall with a shortening after storms, in spring to autumn.

The groundwater level in the 50 m deep borehole B4 is measured in the Northwest-facing slope, at a location covered by the glacier until 2014 and is shown in Figure 8 (red curve). The groundwater level rises during snowmelt

Table 2
Reversible and Irreversible Displacement Across the Valley (ALTS-Reflector Number 2)

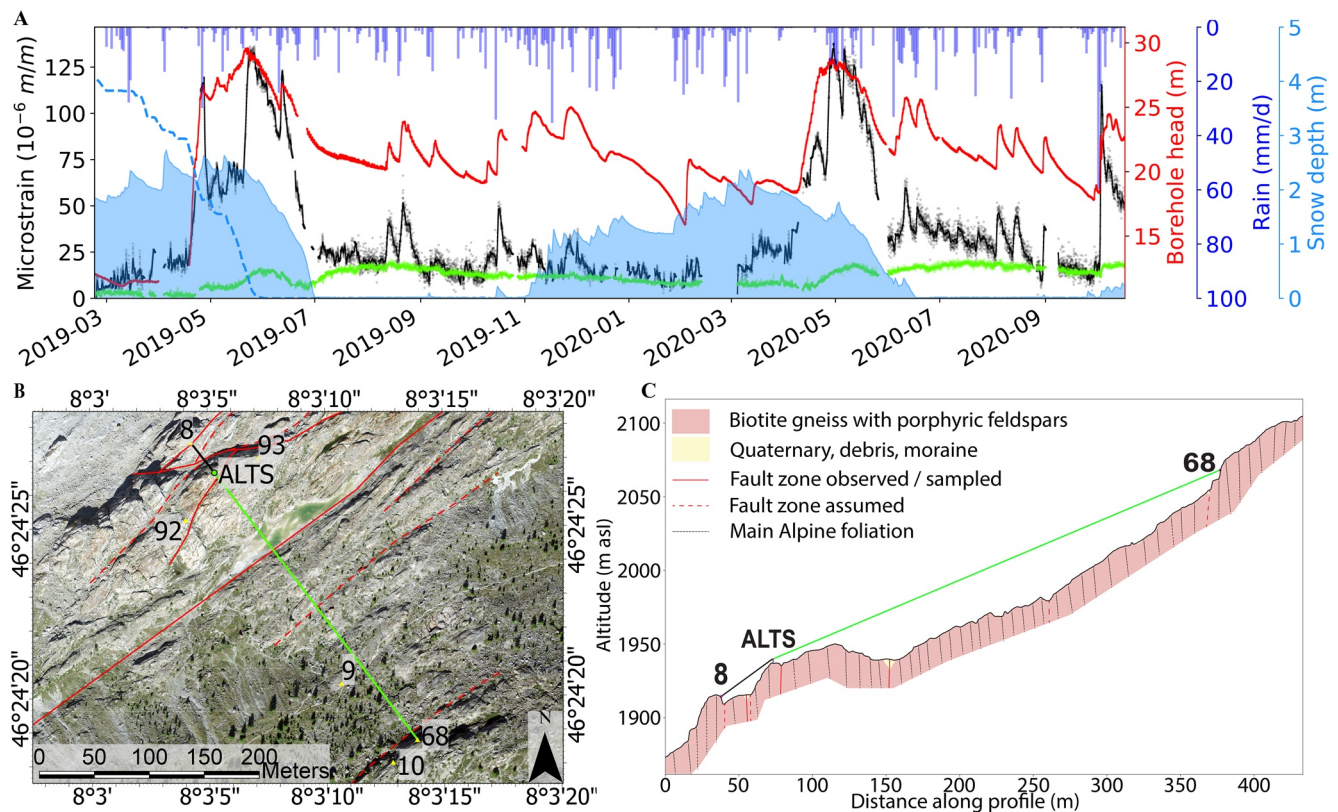| Year	Spring deformation (Microstrains)	Annual non-recovered deformation (Microstrains)
2015	41	7
2016	46	3
2017	36	7
2018	76	35
2019	51	16
2020	39	11

Figure 8. (a) Comparison between the ground deformation (black, reflector 8, green, reflector 68) and the groundwater head in a borehole (red, B4). Rainfall (blue, Bruchji) and snow depth (light blue fill, Eggishorn) are also shown. The dashed dodgerblue line is local SWE around B4 estimated from a time-lapse camera in 2019 (exaggerated 10 times for comparison with snow depth). The camera was not recording in spring 2020 due to technical issues. (b) Map and (c) simplified geologic profile view showing the two lines to reflectors 8 (black) and 68 (green).

in spring and early winter and heavy rainfall in summer and autumn when snow-free conditions prevail. The comparison with ground deformation between the total station and reflector number eight on the same slope exhibits a good match with the groundwater level in the borehole (Pearson's correlation coefficient of 0.74). During winter, exceptions are observed when relatively quick drops in the borehole head with an unusual acceleration over time are not seen in the deformation time series. The deformation between the total station and the reflector 68 is smaller than between the total station and reflector 8, with a much smaller reaction to heavy rainfall events and snowmelt periods. However, the lines to these two points are oriented in the same direction, and the general slope of the surface is similar for both stations (see Figure 8). We observe fault zones, generally oriented parallel to the alpine foliation, and we identify several fault zones crossing the two investigated lines. We note that the density of mapped fault zones is much larger for the section to the reflector 8 than the one to the reflector 68 (see Figure 8).

5. Discussion

5.1. Driving Factors for Reversible Slope Deformations

Deformation signals monitored at different locations worldwide have revealed hydromechanical processes with reversible seasonal patterns. For example, in the Gotthard tunnel in the central Swiss Alps (Hansmann et al., 2012; Loew et al., 2007) and at the long valley caldera in the USA (Silverii et al., 2020), as well as previous studies in the Aletsch valley (Grämiger et al., 2020; Hugentobler et al., 2020). In this study, we show a significant correlation between surface deformation and groundwater storage variations which confirms that pore pressure variations is the main driver for observed rock-slope deformation. We systematically find this control at different spatial and temporal scales, from the borehole to the slope scale and from the rainfall event to the seasonal hydrological cycle. Notably, we find Pearson's correlation coefficients of 0.77 and 0.74 between respectively the IC4 and the groundwater storage from the GR5J model and the groundwater head monitored in the borehole B4

and a nearby reflector (point 8). We confirm that hydromechanical processes linked to the variation in pore pressure control the deformation patterns. At the annual timescale, the ground deformation follows an exponential decay, similarly to the diffusion of pressure during the drainage of an aquifer. By fitting an exponential function as $d(t) = d_0 * \exp(-\frac{t}{\tau})$, where τ is the characteristic decay timescale, d_0 is the deformation at the start of the recession period and $d(t)$ is the evolution of deformation, we found τ to be in the order of a few months (average of 111 ± 46d in Figure 3), similar as the characteristic aquifer drainage timescale found for alpine catchments (Andermann et al., 2012; Brutsaert, 2008; Roques et al., 2021).

While the temperature was observed to drive ground deformation in other places of the Alps (see Section 1 and references therein), modeled thermoelasticity in the Aletsch valley and elsewhere only results in around a millimeter-scale surface deformation (Grämiger et al., 2018). The thermoelastic deformation is expected to influence the measured strain for periods without snow cover insulating the ground, with expansion of the near-surface rocks during warming, resulting in shortening distance across valley flanks in spring, thus adding to the hydromechanical deformation (see Figure 7). However, our results suggest that strong diurnal variations in temperature do not induce significant strain during summer (see e.g., Figure 8) and that the annual peak of deformation systematically occurs before the maximum temperature. Furthermore, the displacement and the strain show a different temporal pattern with respect to temperature, with clear non-sinusoidal behavior. Therefore, we demonstrate that temperature remains a minor driving factor of deformation at the study site.

As mentioned in Section 1, frost-heave in open fractures can also be expected to drive surface deformation. In Aletsch, the rainfall-related deformation occurs with only positive temperatures, excluding frost as a possible driver of this motion. Furthermore, we do not identify episodes of expansion in early winter, and the snowmelt is associated with periods of heave, countering any possible effect of ice thawing in open fractures (see Figure 7).

Hygroscopic expansion happens in meso- and macro-porous material like micro-cracks in gneisses and granites. Hockman and Kessler (1950) have shown that wetting an intact granite in the laboratory leads to an elastic extensional strain of typically 4×10^{-5} (40 microstrains), which is of similar magnitude to the annual cyclic strains recorded in the study area (see Table 2). Near-surface wetting of dry gneisses and granites could occur during rainstorms and possibly snowmelt. However, the time-dependent strains recorded during wetting and drying laboratory experiments (e.g., Hockman & Kessler, 1950; Li et al., 2021) occur on much shorter time scales (e.g., hours) than the annual cyclic deformations monitored in the Aletsch valley. It suggests that the dominant strain signals are related to pressure diffusion and the hydromechanical response of macroscopic permeable structures such as fault zones.

We explore the possibility that a part of the annual elastic deformation observed in the Aletsch valley is caused by the winter snowpack loading the ground surface. We note that the deformability of stiff fractured granite and gneisses is about three orders of magnitudes smaller than for soils. 3 m of average snow depth corresponds to an additional pressure of around 15 kPa on the ground (assuming a snow density of ~500 kg/m³). The snow covers the entire surface, adding a relatively homogeneous load on the ground, although strong spatial variations are observed, with accumulation in depressions and below steep walls, as well as on preferential slope orientations (Lundberg et al., 2016). For a fractured elastic material of 20 GPa stiffness (Zangerl et al., 2008) in the active layer (the top 200 m), the resulting vertical displacement is minimal (~0.1 mm), with progressive subsidence during winter when snow accumulates, and uplift during snowmelt. In mountains, the heterogeneity of snow accumulation due to steep rock faces could induce a minor horizontal component of strain, oriented towards the valley in winter and in the opposite direction during snowmelt. Such small deformations are below the capabilities of our monitoring system. The strain across the valley (Figure 7), as well as the strain between two points of the same slope (Figure 8) do not exhibit a significant change during the first part of the winter when snow accumulates. Thus, the surface deformation by loading from snow appears negligible at our study site.

Among the possible drivers of reversible slope deformation, groundwater-related effect is predominant, as it can explain both seasonal cyclic deformation and short-term excursions following heavy rainfall. We do not exclude other possible drivers but believe their effects are minor compared to varying groundwater heads in the valley slopes.

5.2. Controls on the Spatial Variations in Reversible Deformation

The spatial variations of the annually reversible deformation shown in Figure 2 demonstrate that all reflectors on both sides of the valley move towards the center of the valley in spring, during snowmelt. The orientation of the motion is relatively homogeneous throughout the study area, except for a zone in the North (points 14, 15, 16, AL02) and a zone in the Southwest (points 51–55), where some deviations are visible. The latter group of points is located close to an active landslide, which affects the orientation of the deformation, and the magnitude of the deformation is relatively small, decreasing the signal-to-noise ratio and increasing the uncertainty in the orientation. In the former area (points 14–16, AL02), the valley axis is also rotating, possibly indicating an influence of the topography on the orientation of deformation. However, on the other side of the glacier, the slope orientation is rotated too, but displacements observed at points 17, 18, 19, and AL01 are not perpendicular to the average slope angle around these points. Instead, the displacement direction for this group of points is consistent with the direction of the other points on this side of the valley, with an average horizontal orientation of $328 \pm 7°$. The main alpine foliation has an average dip and dip direction of $85°/137°$ in the valley, with traces of associated shear zones partly visible with the DTM of Figure 2. Hence, the slope is moving perpendicularly to the Alpine foliation and faulting each year.

Figure 8 exhibits details of spatial and temporal differences in deformation at small-scale for two points situated on the same slope. We show that the response to groundwater recharge is heterogeneous in space, with stronger deformation of the line between the reflector 8 and the total station (up to around 100 microstrains for a strong storm event in October 2020) as between the total station and the reflector 68 (only 6 microstrains for the same storm, starting more than 12 hr after the start of ground reaction to point 8). Similarly, during snowmelt, the part of the slope towards point 8 reacts quicker and more than the other line. While the distance between the total station and point 8 (42.6 m) is much smaller than the distance to point 68 (331.0 m), the density of fault zones between the points is larger for the former line. Because the lithology and orientation of foliation are similar for both regions, we believe the fault zones are key to explain the spatial and temporal differences in groundwater-related deformation. We show in Figure 8 that the line to the reflector eight exhibits a quick response to infiltration, and a similar recession as the pressure sensor in the borehole (at ~50 m below ground), while the line to the reflector 68 shows a smaller, slower reaction to summer rainstorms. In addition, both lines exhibit annual cycles with slow recession following snowmelt. The differences highlighted in responses to infiltration and recession shapes could be caused by heterogeneity in the average hydraulic properties of the rockmass.

5.3. Drivers for Long-Term Trends and Rock Mass Fatigue

The cGPS stations in this study exhibit a trend with an uplift of respectively 0.7 mm/yr (ALTD), 1.0 mm/yr (ALTS), 1.6 mm/yr (AL01), 2.6 mm/yr (AL02) compared to the uplift of the reference station HOHT. The station HOHT, situated in the Rhone valley, also has an uplift rate of around 2.1 mm/yr relative to the swiss coordinate reference system CHTRF2016 (http://pnac.swisstopo.admin.ch/pages/en/chtrf.html, last accessed March 2021). We observe that the rates described in this study are in line with previous uplift rates observed in the region (Sternai et al., 2019), and are particularly high for stations closer to the Aletsch glacier. It is expected that the elastic rebound to the current melting of the glacier has a relatively short distance of influence (e.g., Sternai et al., 2019). We indeed find that cGPS stations situated closer to the glacier show larger uplift rates (e.g., AL01, AL02, AL03, ALTS) than stations further away from the current ice body (e.g., ALTD).

We also observe long-term trends towards valley closing, for example, in Figure 7 and in Figure 5, for the independent components 1 and 2. In Figure 7, the rate of closure is around 14.4 μstrain/yr, or 12.6 mm/yr. The irreversible horizontal deformation observed seems to be consistent with damage modeling results of paraglacial slopes under long-term hydromechanical forcing during strong glacier retreat (Grämiger et al., 2020). In addition, it seems that an individual snowmelt season can influence the long-term irreversible deformation of the slope (see, for example, Figure 7). We observe a larger displacement during the 2018 snowmelt season for all monitoring points, and this displacement was not entirely recovered in the following year (see IC 2 on Figure 5). In fact, for the line shown in Figure 7, the trend between 17 October 2014 and 17 October 2017 is 6.2 μstrain/year (against 14.4 μstrain/year if taken until 17 October 2020). We then hypothesize that strong groundwater storage variations caused by high snowmelt infiltration rates may be plausible causes for most of the irreversible deformation. Hydromechanical fatigue could lead to slip along slope parallel preexisting fractures under low effective normal stresses or subcritical propagation of fractures under elevated gravitational shear stress. This observation suggests

that part of the observed long-term trend causing valley closing may be related to hydromecanically controlled slope fatigue, superimposed to the effect of glacier retreat.

6. Conclusions

This study describes and analyzes a unique data set of surface deformation in the Aletsch Valley, Valais, Switzerland, based on two total stations monitoring 93 reflectors, and five continuous GPS stations. The measurements started in the first half of 2014 and are still ongoing in 2021. The time series of these data sets exhibit both long-term deformation trends and annually cyclic displacements.

We can show that the annually cyclic displacements:

1. are oriented towards the valley center and perpendicular to the main alpine foliation during spring at almost all stations where this type of motion could be observed (Figure 2).
2. show a peak-to-peak displacement magnitude of up to 3.8 cm (Figures 3 and 2).
3. correlate in magnitude with snow height and (meltwater equivalent) at the beginning of spring groundwater recharge period (Figure 7).
4. are correlated to catchment-scale groundwater storage-discharge dynamics computed with a simple lumped rainfall-runoff model, as well as with local pore pressure measurements (Figure 6).

Groundwater-induced surface displacements can also be observed following short-term recharge periods, such as summer rainfall events (Figures 7 and 8). Both the annual displacement caused by spring snowmelt and short-term displacements caused by rainfall events correlate with groundwater level time series in the nearby borehole. Therefore, we conclude that the reversible surface displacements are mainly caused by variations of groundwater heads in the granitic and gneissic rock mass. Minor additional contributions from thermoelastic strains, hygroscopic expansion and snow loading can not be excluded, but we show that these effects must induce only minor displacement magnitudes in the Aletsch valley.

In the study area, the deformation is relatively homogeneous at the slope-scale (Figure 2), but can exhibit significant variations locally (Figure 8). Short-distance measurements show that deformation is heterogeneous in space, with substantially increased strain close to steeply dipping brittle-ductile fault zones. We hypothesize that some of the larger-scale fault zones are a significant source of groundwater-induced strain in the slopes.

Long-term trends in the surface displacement time series are observed consisting of (a) long-term differential uplift close to the glacier border (in the order of 1 mm/yr to 3 mm/yr) and (b) horizontal slope displacements (in the order of 1 mm/yr to 10 mm/yr for points out of mapped active instabilities) leading to a progressive closure of the valley (see Figures 3 and 7). The first trend can be related to isostatic elastic rebound after long term glacier ice downwasting. The irreversible horizontal displacements can be explained by slope damage and shear along critically oriented fractures, driven by rock mass fatigue from annual hydromechanical loading. We can relate the magnitude of peak-to-peak annual displacement with the amount of non-recovered displacement per year for measurements across the valley (Figure 7 and Table 2). Longer time series and further investigations are needed to confirm this hypothesis.

Appendix A: Rainfall-Runoff Model GR5J

The lumped rainfall-runoff model GR5J takes as inputs the flow in the river, air temperature, total precipitation, and sunshine duration. To minimize the impact of the glaciers on the modeled groundwater store, we calibrate the model on periods when the average filtered temperature at the Jungfraujoch station drops below −7°C. The calibration periods are shown in green in Figure 4. During summer, the strong diurnal variations and high water flow in the Massa river are mainly attributable to melting ice. They peak in the late afternoon and correlate with air temperature in the valley. Additionally, the difference between observed and modeled Massa river flow has a similar order of magnitude as the contribution from the melting of the glacier, which is approximately 10 m of ice loss per year.

Figure A1.

The analysis of the frequency content of the river flow data set (Figure A2) is performed on the data between 1974 and 2020 when the sampling interval was 5 min. A clear annual cyclicity and semiannual (and less clear terannual) oscillations are visible and can be linked to the seasonality in temperature and the impact of snowmelt, glacier melt, and groundwater fluctuations. Daily cycles and their multiples are also seen in the time series, and correspond to daily fluctuations of glacier melt in summer, with higher flow in the late afternoon and early night and lower flow in the early morning. These daily oscillations are not observed during winter. For these reasons, we believe that the contribution of the glaciers to the flow in the river is minimal during winter.
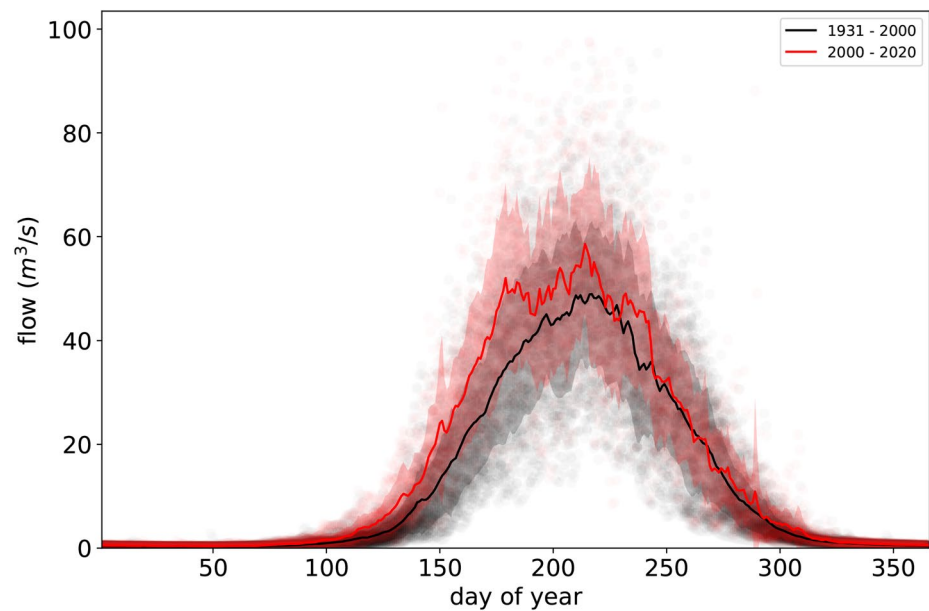

Figure A1. Daily mean flow in cubic meters per second at the Massa river monitoring station per day of the year. Black dots are daily data points between 1931 and 1999; red dots are data points between 2000 and 2020. Lines are mean per day of the year, and fill is the standard deviation.
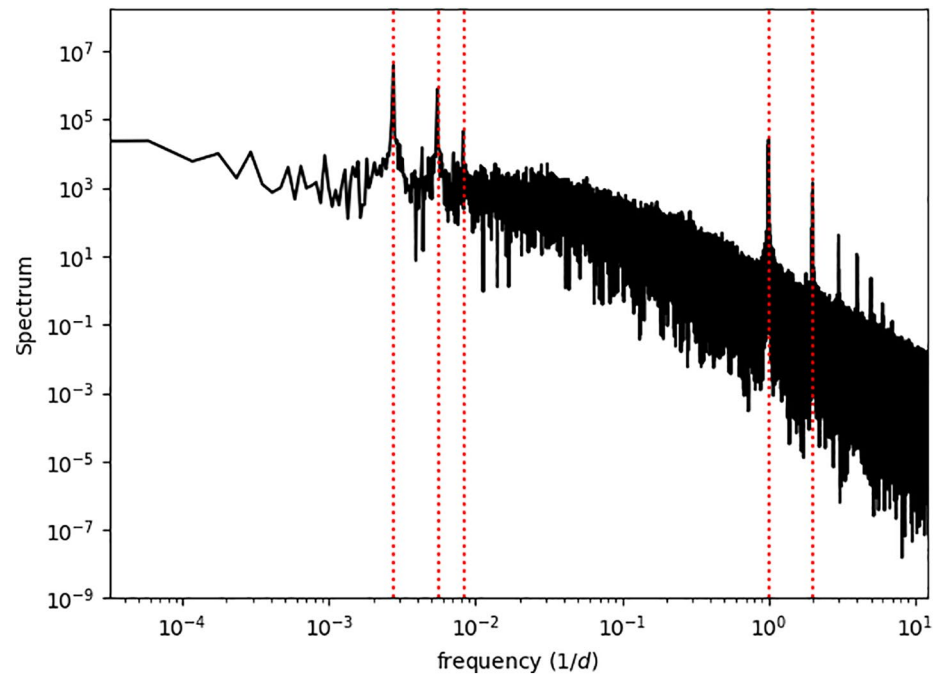
Figure A2. Periodogram of the hourly measurements of the flow in the Massa River since 1974 (start of sub-daily measurements at the flow gauge). The power spectral density is shown versus frequency in cycles per day with a logarithmic scale. Red dashed lines correspond to cycles with periods of 365d, 180d, 120d, 1d and 0.5d.

Appendix B: Correlation Between Deformation and Environmental Factors

To help with the interpretation of the datasets and as a tool to determine which environmental factors could cause the observed deformation time series, we show the Pearson's correlation coefficients of correlation between time series in Figure B1. In Figure B2 we show the correlation matrix between:

1. The water flow in cubic meters per second measured at the Massa River flow gauge;
2. The snow depth in centimeters measured at the Eggishorn weather station;
3. The near-surface air temperature in degree Celsius at the Chatzulecher station;
4. The atmospheric pressure in hectopascals;
5. The groundwater store modeled from GR5J in millimeters;
6. The infiltration from snowmelt and rainfall, modeled from GR5J in millimeters;
7. The snowmelt modeled from GR5J in millimeters;
8. The four independent components of deformation identified from the vbICA analysis.

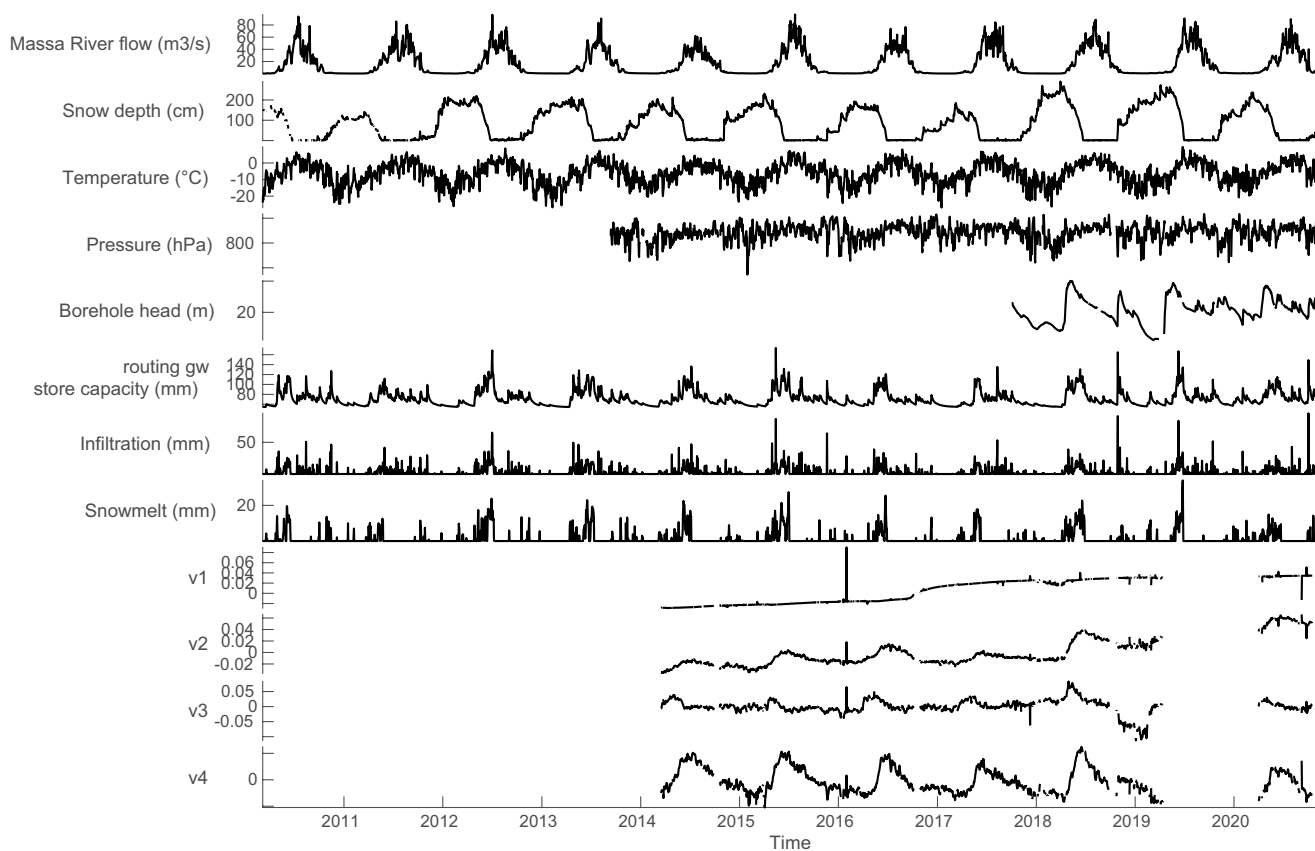**Figure B1.** Data set used for the correlation matrix, with river flow in the Massa river, snow depth at the Eggishorn station, temperature at the Jungfraujoch station, atmospheric pressure at the Chatzulecher station, observed groundwater head in the borehole B4, modeled groundwater store, infiltration and snowmelt from the GR5J model (Figure 4), as well as the four independent components of the vbICA (Figure 5).
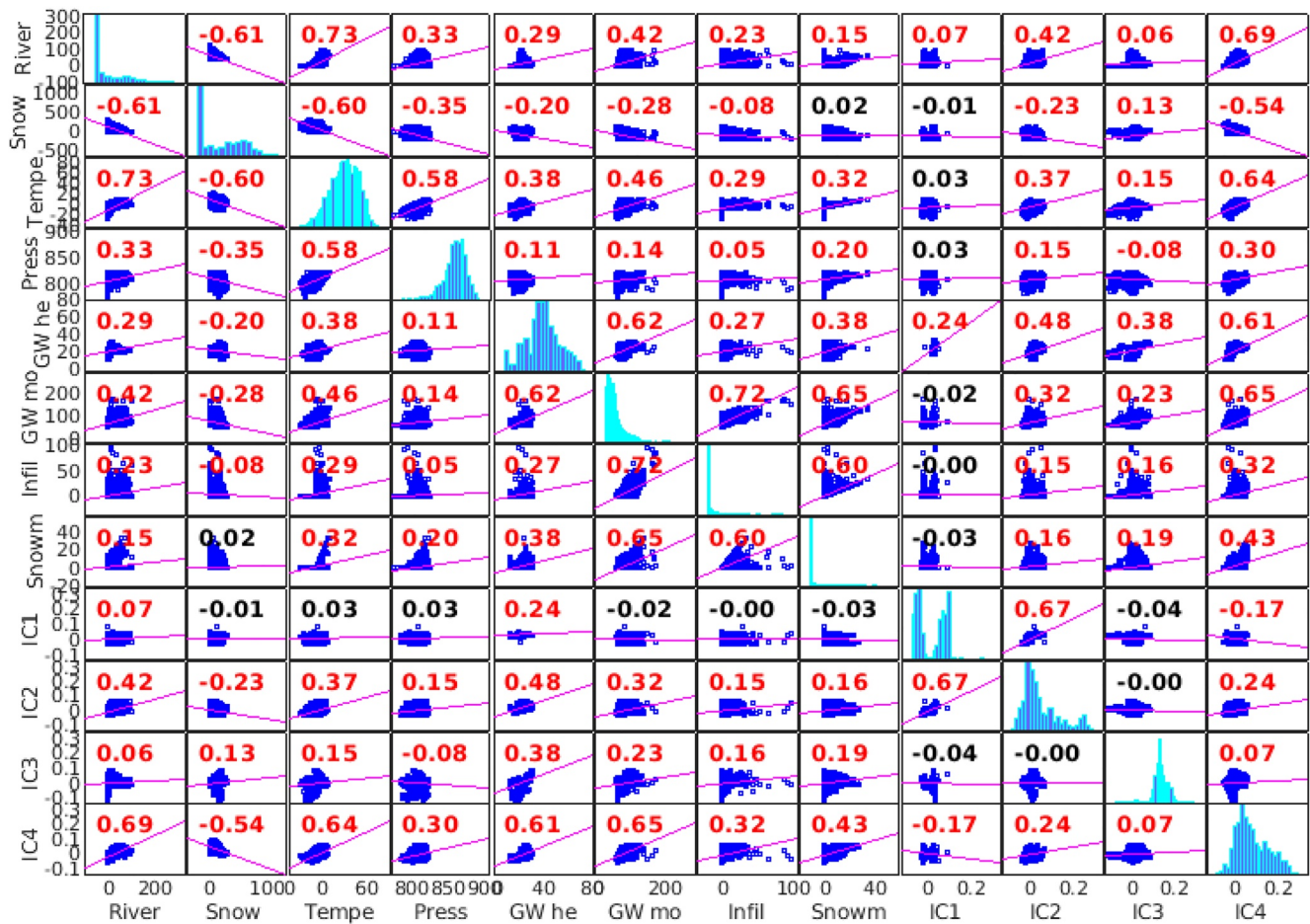
Figure B2. Correlation matrix (Pearson's correlation coefficients) between the time series from Figure B2. Histograms of individual inputs are shown on the diagonal.

Appendix C: Correction of GPS Data

The analysis presented in this paper uses HOHT (Hohtenn) as a reference station. This station (green triangle on Figure C1), part of the Swisstopo AGNES network of GNSS stations, is in the Rhone valley, more than 20 km away from our study area. Therefore, the baseline to this station from the single frequency station installed in the Aletsch valley would be too long. Instead, we reference the stations used in this study to the FIES station, at a shorter distance of less than 8 km. The FIES station is itself referenced to HOHT. For the sake of clarity, we show on Figure C1 the three components of displacement at the station Fies (relative to HOHT) in red, ALTS (Chatzulecher, relative to FIES) in green, as well as the resulting correction of ALTS relative to HOHT in black. It is clear in this figure that the station FIES is subjected to similar types of motion as the stations used in this study, but is situated on the opposite side of the mountain range, therefore exhibiting a motion in spring to the South-East, similarly to ALTD and AL02.
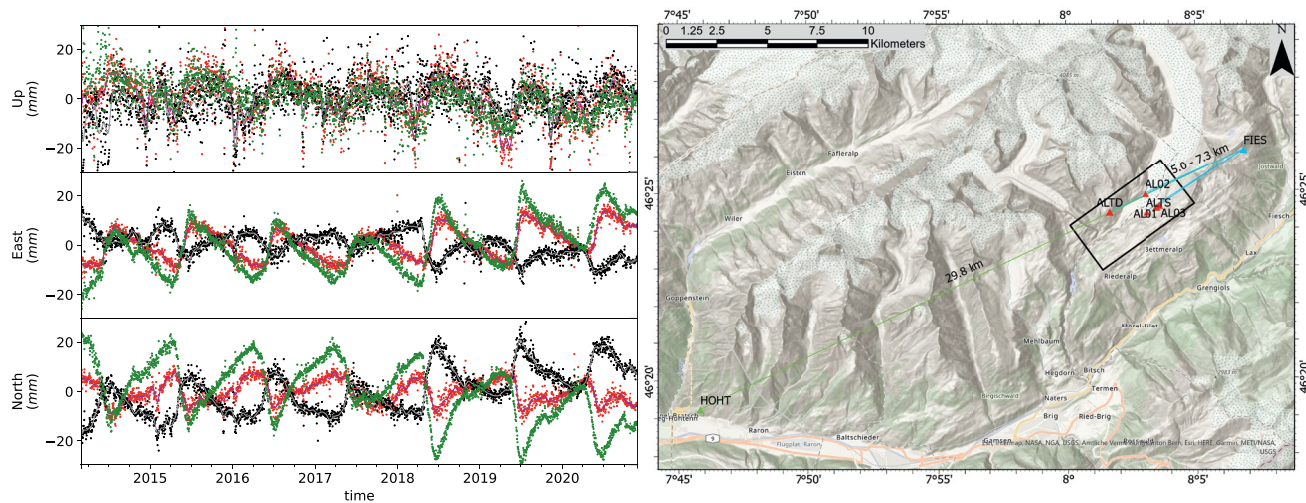
Figure C1. Three components of displacement of ALTS (black) and FIES (red) continuous Global Positioning System stations relative to HOHT. ALTS relative to FIES (green) represents the baseline between the station, before correction with the displacement of FIES relative to HOHT. The baselines between the single frequency stations used in this study (red triangles) and FIES (blue triangle) as well as the baseline between FIES and HOHT (green triangle) are displayed on a regional map. Black rectangle is the extent of Figure 2.

Data Availability Statement

The displacement data used in this study are available through the ETH Research Collections: https://doi.org/10.3929/ethz-b-000494451, last accessed in November 2021.

References

Aaron, J., Loew, S., & Forrer, M. (2021). Recharge response and kinematics of an unusual earthflow in Liechtenstein. *Landslides*, *3*, 2383–2401. https://doi.org/10.1007/s10346-021-01633-5

Andermann, C., Longuevergne, L., Bonnet, S., Crave, A., Davy, P., & Gloaguen, R. (2012). Impact of transient groundwater storage on the discharge of Himalayan Rivers. *Nature Geoscience*, *5*(2), 127–132. https://doi.org/10.1038/ngeo1356

Bettinelli, P., Avouac, J. P., Flouzat, M., Bollinger, L., Ramillien, G., Rajaure, S., & Sapkota, S. (2008). Seasonal variations of seismicity and geodetic strain in the Himalaya induced by surface hydrology. *Earth and Planetary Science Letters*, *266*, 332–344. https://doi.org/10.1016/j.epsl.2007.11.021

Biot, M. A. (1941). General theory of three-dimensional consolidation. *Journal of Applied Physics*, *12*(2), 155–164. https://doi.org/10.1063/1.1712886

Braitenberg, C., Pivetta, T., Barbolla, D. F., Gabrovšek, F., Devoti, R., & Nagy, I. (2019). Terrain uplift due to natural hydrologic overpressure in karstic conduits. *Scientific Reports*, *9*(1), 3934. https://doi.org/10.1038/s41598-019-38814-1

Brutsaert, W. (2008). Long-term groundwater storage trends estimated from streamflow records: Climatic perspective. *Water Resources Research*, *44*(2), 1–7. https://doi.org/10.1029/2007WR006518

Chanard, K., Avouac, J. P., Ramillien, G., & Genrich, J. (2014). Modeling deformation induced by seasonal variations of continental water in the Himalaya region: Sensitivity to Earth elastic structure. *Journal of Geophysical Research: Solid Earth*, *119*(6), 5097–5113. https://doi.org/10.1002/2013JB010451

Choudrey, R. A., & Roberts, S. J. (2003). Variational mixture of Bayesian independent component analyzers. *Neural Computation*, *15*(1), 213–252. https://doi.org/10.1162/089976603321043766

Cody, E., Anderson, B. M., McColl, S. T., Fuller, I. C., & Purdie, H. L. (2020). Paraglacial adjustment of sediment slopes during and immediately after glacial debuttressing. *Geomorphology*, *371*, 107411. https://doi.org/10.1016/j.geomorph.2020.107411

Collins, B. D., & Stock, G. M. (2016). Rockfall triggering by cyclic thermal stressing of exfoliation fractures. *Nature Geoscience*, *9*, 395–400. https://doi.org/10.1038/ngeo2686

Collins, B. D., Stock, G. M., Eppes, M. C., Lewis, S. W., Corbett, S. C., & Smith, J. B. (2018). Thermal influences on spontaneous rock dome exfoliation. *Nature Communications*, *9*(1), 1–12. https://doi.org/10.1038/s41467-017-02728-1

de Palézieux, L., & Loew, S. (2019). Long-term transient groundwater pressure and deep infiltration in Alpine mountain slopes (Poschiavo Valley, Switzerland). *Hydrogeology Journal*, *27*(8), 2817–2834. https://doi.org/10.1007/s10040-019-02025-9

Drouin, V., Heki, K., Sigmundsson, F., Hreinsdóttir, S., & Ófeigsson, B. G. (2016). Constraints on seasonal load variations and regional rigidity from continuous GPS measurements in Iceland, 1997-2014. *Geophysical Journal International*, *205*(3), 1843–1858. https://doi.org/10.1093/gji/ggw122

Eberhardt, E., Stead, D., & Coggan, J. (2004). Numerical analysis of initiation and progressive failure in natural rock slopes—The 1991 Randa rockslide. *International Journal of Rock Mechanics and Mining Sciences*, *41*(1), 69–87. https://doi.org/10.1016/S1365-1609(03)00076-5

Flouzat, M., Bettinelli, P., Willis, P., Avouac, J.-P., Héritier, T., & Gautam, U. (2009). Investigating tropospheric effects and seasonal position variations in GPS and DORIS time-series from the Nepal Himalaya. *Geophysical Journal International*, *178*(3), 1246–1259. https://doi.org/10.1111/j.1365-246X.2009.04252.x

Frukacz, M., Presl, R., Wieser, A., & Favot, D. (2017). Pushing the sensitivity limits of RTS-based continuous deformation monitoring of an alpine valley. *Applied Geomatics*, *9*(2), 81–92. https://doi.org/10.1007/s12518-017-0182-2

Gahalaut, V. K., Yadav, R. K., Sreejith, K. M., Gahalaut, K., Bürgmann, R., Agrawa, R., et al. (2017). InSAR and GPS measurements of crustal deformation due to seasonal loading of Tehri reservoir in Garhwal Himalaya, India. *Geophysical Journal International*, *209*(1), 425–433. https://doi.org/10.1093/gji/ggx015

Gautam, P. K., Gahalaut, V., Prajapati, S. K., Kumar, N., Yadav, R. K., Rana, N., & Dabral, C. P. (2017). Continuous GPS measurements of crustal deformation in Garhwal-Kumaun Himalaya. *Quaternary International*, *462*, 124–129. https://doi.org/10.1016/j.quaint.2017.05.043

Girard, L., Gruber, S., Weber, S., & Beutel, J. (2013). Environmental controls of frost cracking revealed through in situ acoustic emission measurements in steep bedrock. *Geophysical Research Letters*, *40*(9), 1748–1753. https://doi.org/10.1002/grl.50384

Gischig, V. S., Moore, J. R., Evans, K. F., Amann, F., & Loew, S. (2011). Thermomechanical forcing of deep rock slope deformation: 2. The Randa rock slope instability. *Journal of Geophysical Research: Earth Surface*, *116*(F4), F04011. https://doi.org/10.1029/2011JF002007

GLAMOS. (2020). Swiss glacier length change, release 2020, glacier monitoring Switzerland. https://doi.org/10.18750/lengthchange.2020.r2020

Glueer, F., Loew, S., & Manconi, A. (2020). Paraglacial history and structure of the Moosfluh Landslide (1850–2016), Switzerland. *Geomorphology*, *355*, 106677. https://doi.org/10.1016/j.geomorph.2019.02.021

Glueer, F., Loew, S., Manconi, A., & Aaron, J. (2019). From toppling to sliding: Progressive evolution of the Moosfluh Landslide, Switzerland. *Journal of Geophysical Research: Earth Surface*, *124*(12), 2899–2919. https://doi.org/10.1029/2019JF005019

Glueer, F., Loew, S., Seifert, R., Aaron, J., Grämiger, L., Conzett, S., et al. (2021). Robotic total station monitoring in high alpine paraglacial environments: Challenges and solutions from the Great Aletsch region (Valais, Switzerland). *Geosciences*, *11*(11), 471. https://doi.org/10.3390/geosciences11110471

Grämiger, L. M., Moore, J. R., Gischig, V. S., Ivy-Ochs, S., & Loew, S. (2017). Beyond debuttressing: Mechanics of paraglacial rock slope damage during repeat glacial cycles. *Journal of Geophysical Research: Earth Surface*, *122*(4), 1004–1036. https://doi.org/10.1002/2016JF003967

Grämiger, L. M., Moore, J. R., Gischig, V. S., & Loew, S. (2018). Thermomechanical stresses drive damage of Alpine valley rock walls during repeat glacial cycles. *Journal of Geophysical Research: Earth Surface*, *123*(10), 2620–2646. https://doi.org/10.1029/2018JF004626

Grämiger, L. M., Moore, J. R., Gischig, V. S., Loew, S., Funk, M., & Limpach, P. (2020). Hydromechanical rock slope damage during late Pleistocene and Holocene glacial cycles in an Alpine Valley. *Journal of Geophysical Research: Earth Surface*, *125*(8), 1–24. https://doi.org/10.1029/2019JF005494

Grillo, B., Braitenberg, C., Nagy, I., Devoti, R., Zuliani, D., & Fabris, P. (2018). Cansiglio Karst Plateau: 10 years of geodetic-hydrological observations in seismically active Northeast Italy. *Pure and Applied Geophysics*, *175*(5), 1765–1781. https://doi.org/10.1007/s00024-018-1860-7

Gruber, S., & Haeberli, W. (2007). Permafrost in steep bedrock slopes and its temperature-related destabilization following climate change. *Journal of Geophysical Research*, *112*(F2), F02S18. https://doi.org/10.1029/2006JF000547

Gualandi, A., & Liu, Z. (2021). Variational Bayesian independent component analysis for InSAR displacement time-series with application to Central California, USA. *Journal of Geophysical Research: Solid Earth*, *126*(4), e2020JB020845. https://doi.org/10.1029/2020JB020845

Gualandi, A., Serpelloni, E., & Belardinelli, M. E. (2016). Blind source separation problem in GPS time series. *Journal of Geodesy*, *90*(4), 323–341. https://doi.org/10.1007/s00190-015-0875-4

Hansmann, J., Loew, S., & Evans, K. F. (2012). Reversible rock-slope deformations caused by cyclic water-table fluctuations in mountain slopes of the Central Alps, Switzerland. *Hydrogeology Journal*, *20*(1), 73–91. https://doi.org/10.1007/s10040-011-0801-7

Heki, K. (2001). Seasonal modulation of interseismic strain buildup in Northeastern Japan driven by snow loads. *Science*, *293*(5527), 89–92. https://doi.org/10.1126/science.1061056

Hockman, A., & Kessler, D. W. (1950). Thermal and moisture expansion studies of some domestic granites. *Journal of Research of the National Bureau of Standards*, *44*, 395–410. https://doi.org/10.6028/jres.044.035

Hugentobler, M., Loew, S., Aaron, J., Roques, C., & Oestreicher, N. (2020). Borehole monitoring of thermo-hydro-mechanical rock slope processes adjacent to an actively retreating glacier. *Geomorphology*, *362*, 107190. https://doi.org/10.1016/j.geomorph.2020.107190

Ivy-Ochs, S., Kerschner, H., Reuther, A., Preusser, F., Heine, K., Maisch, M., et al. (2008). Chronology of the last glacial cycle in the European Alps. *Journal of Quaternary Science*, *23*(6–7), 559–573. https://doi.org/10.1002/jqs.1202

Jiang, Y., Dixon, T. H., & Wdowinski, S. (2010). Accelerating uplift in the North Atlantic region as an indicator of ice loss. *Nature Geoscience*, *3*(6), 404–407. https://doi.org/10.1038/ngeo845

Kos, A., Amann, F., Strozzi, T., Delaloye, R., von Ruette, J., & Springman, S. (2016). Contemporary glacier retreat triggers a rapid landslide response, Great Aletsch Glacier. *Geophysical Research Letters*, *43*, 12466–12474. https://doi.org/10.1002/2016GL071708

Leica Geosystems, AG. (2013). *Leica MS50/TS50/TM50 user manual v1.1.1*. Retrieved from http://surveyequipment.com/assets/index/download/id/219/

Leith, K., Moore, J. R., Amann, F., & Loew, S. (2014). Subglacial extensional fracture development and implications for Alpine Valley evolution. *Journal of Geophysical Research: Earth Surface*, *119*(1), 62–81. https://doi.org/10.1002/2012JF002691

Li, Y., Leith, K., Perras, M., & Loew, S. (2021). Digital image correlation–based analysis of hygroscopic expansion in Herrnholz granite. *International Journal of Rock Mechanics and Mining Sciences*, *146*, 104859. https://doi.org/10.1016/j.ijrmms.2021.104859

Limpach, P., Geiger, A., & Raetzo, H. (2016). GNSS for Deformation and Geohazard Monitoring in the Swiss Alps. In *Proceedings of the 3rd joint international symposium on deformation monitoring (jisdm 2016)*. (pp. 1–4).

Loew, S., Ebneter, F., Bremen, R., Herfort, M., Lützenkirchen, V., & Matousek, F. (2007). Annual opening and closure of Alpine Valleys. *Felsbau: Rock and Soil Engineering*, *25*(5), 1–60. Retrieved from https://structurae.net/en/literature/journal-article/annual-opening-and-closure-of-alpine-valleys

Loew, S., Grämiger, L., Gischig, V., Glüer, F. & Gschwind, S. (2017). *Progressive failure of brittle rock slopes: Field observations, modeling results and unknowns*, ISRM Progressive Rock Failure Conference.

Ludwigsen, C. A., Khan, S. A., Andersen, O. B., & Marzeion, B. (2020). Vertical land motion from present-day deglaciation in the Wider Arctic. *Geophysical Research Letters*, *47*(19), 1–11. https://doi.org/10.1029/2020GL088144

Lundberg, A., Ala-Aho, P., Eklo, O., Klöve, B., Kværner, J., & Stumpp, C. (2016). Snow and frost: Implications for spatiotemporal infiltration patterns–A review. *Hydrological Processes*, *30*(8), 1230–1250. https://doi.org/10.1002/hyp.10703

Mann, M. E., Zhang, Z., Rutherford, S., Bradley, R. S., Hughes, M. K., Shindell, D., et al. (2009). Global Signatures and dynamical origins of the little ice age and medieval climate anomaly. *Science*, *326*(5957), 1256–1260. https://doi.org/10.1126/science.1177303

Marmoni, G. M., Fiorucci, M., Grechi, G., & Martino, S. (2020). Modelling of thermo-mechanical effects in a rock quarry wall induced by near-surface temperature fluctuations. *International Journal of Rock Mechanics and Mining Sciences*, *134*(May 2019), 104440. https://doi.org/10.1016/j.ijrmms.2020.104440

Masset, O., & Loew, S. (2010). Hydraulic conductivity distribution in crystalline rocks, derived from inflows to tunnels and galleries in the Central Alps, Switzerland. *Hydrogeology Journal*, *18*(4), 863–891. https://doi.org/10.1007/s10040-009-0569-1

Matsuoka, N. (2008). Frost weathering and rockwall erosion in the southeastern Swiss Alps: Long-term (1994–2006) observations. *Geomorphology*, *99*(1–4), 353–368. https://doi.org/10.1016/j.geomorph.2007.11.013

McColl, S. T. (2012). Paraglacial rock-slope stability. *Geomorphology*, *153–154*, 1–16. https://doi.org/10.1016/J.GEOMORPH.2012.02.015

Mey, J., Scherler, D., Wickert, A. D., Egholm, D. L., Tesauro, M., Schildgen, T. F., & Strecker, M. R. (2016). Glacial isostatic uplift of the European Alps. *Nature Communications*, *7*(1), 13382. https://doi.org/10.1038/ncomms13382

Moreira, D. M., Calmant, S., Perosanz, F., Xavier, L., Rotunno Filho, O. C., Seyler, F., & Monteiro, A. C. (2016). Comparisons of observed and modeled elastic responses to hydrological loading in the Amazon basin. *Geophysical Research Letters*, *43*(18), 9604–9610. https://doi.org/10.1002/2016GL070265

Muelchi, R., Rössler, O., Schwanbeck, J., Weingartner, R., & Martius, O. (2021). River runoff in Switzerland in a changing climate–Runoff regime changes and their time of emergence. *Hydrology and Earth System Sciences*, *25*(6), 3071–3086. https://doi.org/10.5194/hess-25-3071-2021

Musso Piantelli, F., Herwegh, M., Anselmetti, F. S., Waldvogel, M., & Gruner, U. (2020). Microfracture propagation in gneiss through frost wedging: Insights from an experimental study. *Natural Hazards*, *100*(2), 843–860. https://doi.org/10.1007/s11069-019-03846-3

Nash, J., & Sutcliffe, J. (1970). River flow forecasting through conceptual models part I—A discussion of principles. *Journal of Hydrology*, *10*(3), 282–290. https://doi.org/10.1016/0022-1694(70)90255-6

Oestreicher, N. (2018). *Geodetic, hydrologic and seismological signals associated with precipitation and infiltration in the central Southern Alps* [Thesis, Victoria University of Wellington] Retrieved from http://researcharchive.vuw.ac.nz/handle/10063/7024

Pintori, F., Serpelloni, E., Longuevergne, L., Garcia, A., Faenza, L., D'Alberto, L., et al. (2021). Mechanical response of shallow crust to groundwater storage variations: Inferences from deformation and seismic observations in the Eastern Southern Alps, Italy. *Journal of Geophysical Research: Solid Earth*, e2020JB020586. *126*. https://doi.org/10.1029/2020JB020586

Prawirodirdjo, L., Ben-Zion, Y., & Bock, Y. (2006). Observation and modeling of thermoelastic strain in Southern California Integrated GPS Network daily position time series. *Journal of Geophysical Research: Solid Earth*, *111*(B2), B02408. https://doi.org/10.1029/2005JB003716

Pushpalatha, R., Perrin, C., Le Moine, N., Mathevet, T., & Andréassian, V. (2011). A downward structural sensitivity analysis of hydrological models to improve low-flow simulation. *Journal of Hydrology*, *411*(1–2), 66–76. https://doi.org/10.1016/j.jhydrol.2011.09.034

Rango, A., & Martinec, J. (1995). Revisiting the degree-day method for snowmelt computation. *JAWRA Journal of the American Water Resources Association*, *31*, 657–669. https://doi.org/10.1111/j.1752-1688.1995.tb03392.x

Rice, J. R., & Cleary, M. P. (1976). Some basic stress diffusion solutions for fluid-saturated elastic porous media with compressible constituents. *Reviews of Geophysics*, *14*(2), 227. https://doi.org/10.1029/RG014i002p00227

Roques, C., Lacroix, S., Leith, K., Longuevergne, L., Leray, S., Jachens, E. R., et al. (2021). *Geomorphological and geological controls on storage-discharge functions of alpine landscapes: Evidence from streamflow analysis in the Swiss Alps and perspectives for the critical zone community*. Earth's Future. https://doi.org/10.1002/ESSOAR.10506976.1

Schaltegger, U. (1994). Unravelling the pre-Mesozoic history of Aar and Gotthard massifs (Central Alps) by isotopic dating: A review. *Schweizerische mineralogische und petrographische Mitteilungen*, *74*(1), 41–51. https://doi.org/10.5169/seals-56330

Serpelloni, E., Pintori, F., Gualandi, A., Scoccimarro, E., Cavaliere, A., Anderlini, L., et al. (2018). Hydrologically induced Karst Deformation: Insights from GPS measurements in the Adria-Eurasia Plate Boundary Zone. *Journal of Geophysical Research: Solid Earth*, *123*, 4413–4430. https://doi.org/10.1002/2017JB015252

Silverii, F., D'Agostino, N., Borsa, A. A., Calcaterra, S., Gambino, P., Giuliani, R., & Mattone, M. (2019). Transient crustal deformation from karst aquifers hydrology in the Apennines (Italy). *Earth and Planetary Science Letters*, *506*, 23–37. https://doi.org/10.1016/j.epsl.2018.10.019

Silverii, F., Montgomery-Brown, E. K., Borsa, A. A., & Barbour, A. J. (2020). Hydrologically induced deformation in long valley Caldera and Adjacent Sierra Nevada. *Journal of Geophysical Research: Solid Earth*, *125*(5), e2020JB019495. https://doi.org/10.1029/2020JB019495

Steck, A. (1983). Geologie Der Aletschregion (Vs). *Bulletin de la Murithienne*, *101*, 135–154.

Sternai, P., Sue, C., Husson, L., Serpelloni, E., Becker, T. W., Willett, S. D., et al. (2019). Present-day uplift of the European Alps: Evaluating mechanisms and models of their relative contributions. *Earth-Science Reviews*, *190*, 589–604. https://doi.org/10.1016/j.earscirev.2019.01.005

Strozzi, T., Delaloye, R., Kääb, A., Ambrosi, C., Perruchoud, E., & Wegmüller, U. (2010). Combined observations of rock mass movements using satellite SAR interferometry, differential GPS, airborne digital photogrammetry, and airborne photography interpretation. *Journal of Geophysical Research: Earth Surface*, *115*, F01014. https://doi.org/10.1029/2009JF001311

Tsai, V. C. (2011). A model for seasonal changes in GPS positions and seismic wave speeds due to thermoelastic and hydrologic variations. *Journal of Geophysical Research*, *116*(B4), B04404. https://doi.org/10.1029/2010JB008156

Turc, L. (1961). Evaluation des besoins en eau d'irrigation, evapotranspiration potentielle. *Annals of Agronomy*, *12*, 13–49. Retrieved from https://ci.nii.ac.jp/naid/20000722287

Ustaszewski, M. E., Hampel, A., & Pfiffner, O. A. (2008). Composite faults in the Swiss Alps formed by the interplay of tectonics, gravitation and postglacial rebound: An integrated field and modelling study. *Swiss Journal of Geosciences*, *101*(1), 223–235. https://doi.org/10.1007/s00015-008-1249-1

Valéry, A., Andréassian, V., & Perrin, C. (2014). 'As simple as possible but not simpler': What is useful in a temperature-based snow-accounting routine? Part 2–Sensitivity analysis of the Cemaneige snow accounting routine on 380 catchments. *Journal of Hydrology*, *517*, 1176–1187. https://doi.org/10.1016/j.jhydrol.2014.04.058

Van Dam, T., Wahr, J., Milly, P. C., Shmakin, A. B., Blewitt, G., Lavallée, D., & Larson, K. M. (2001). Crustal displacements due to continental water loading. *Geophysical Research Letters*, *28*(4), 651–654. https://doi.org/10.1029/2000GL012120

Wang, H. F. (2000). *Theory of linear poroelasticity with applications to geomechanics and hydrogeology*. Princeton University Press. Retrieved from https://press.princeton.edu/titles/7006.html

Weber, S., Beutel, J., Da Forno, R., Geiger, A., Gruber, S., Gsell, T., et al. (2019). A decade of detailed observations (2008–2018) in steep bedrock permafrost at the Matterhorn Hörnligrat (Zermatt, CH). *Earth System Science Data*, *11*(3), 1203–1237. https://doi.org/10.5194/essd-11-1203-2019

Weber, S., Beutel, J., Faillettaz, J., Hasler, A., Krautblatter, M., & Vieli, A. (2017). Quantifying irreversible movement in steep, fractured bedrock permafrost on Matterhorn (CH). *The Cryosphere*, *11*(1), 567–583. https://doi.org/10.5194/tc-11-567-2017

Wegmann, M., & Gudmundsson, G. H. (1999). Thermally induced temporal strain variations in rock walls observed at subzero temperatures. In K. Hutter, Y. Wang, & H. Beer (Eds.), *Advances in cold-region thermal engineering and sciences* (pp. 511–518). Springer Berlin Heidelberg.

Zangerl, C., Eberhardt, E., Evans, K., & Loew, S. (2008). Consolidation settlements above deep tunnels in fractured crystalline rock: Part 2—Numerical analysis of the Gotthard highway tunnel case study. *International Journal of Rock Mechanics and Mining Sciences*, *45*(8), 1211–1225. https://doi.org/10.1016/j.ijrmms.2008.02.005